Light-sheet fluorescence microscopy

UNIVERSITÉ DE STRASBOURG

ÉCOLE DOCTORALE

DES SCIENCES DE LA VIE ET DE LA SANTE

Institut de génétique et de biologie moléculaire et cellulaire (IGBMC)
UMR 7104/UMR_S 1258

THÈSE

présentée par :

Elena REMACHA MOTTA

soutenue le : **08 septembre 2020**

pour obtenir le grade de : **Docteur de l'université de Strasbourg**

Discipline/ Spécialité : Biophysics

Développement de stratégies de microscopie pour l'imagerie rapide du développement du cœur du poisson-zèbre

THÈSE dirigée par :

Dr. VERMOT Julien	DR2, Université de Strasbourg – IGBMC, FR
Dr. FAHRBACH Florian	Leica Microsystems, DE

RAPPORTEURS :

Dr. SUPATTO Willy	CR, École polytechnique – CNRS, FR
Dr. MERCADER HUBER Nadia	PR, University of Bern, CH

AUTRES MEMBRES DU JURY :

Dr. DIDIER Pascal	PR, Université de Strasbourg – UDS, FR
Dr. RIVELINE Daniel	DR, Université de Strasbourg – CNRS, FR

Acknowledgements

Firstly, I would like to thank my advisors Dr. Florian Fahrbach and Dr. Julien Vermot, for the continuous support of my Ph.D. study and related research, for his patience, motivation, and immense knowledge. His guidance helped me in all the time of research and writing of this thesis.

Besides my advisors, I would like to thank the rest of my thesis committee: Dr. Willy Supatto, Dr. Nadia Mercader Huber, Dr. Pascal Didier, and Dr. Daniel Riveline for accepting to evaluate my work.

I thank my labmates for the discussions and constant support: Laia, Helene, Renee, Pedro, Marina, and Hajime. Also, I thank my friends in IGBMC, for making every day in the lab more enjoyable.

Last but not the least, I would like to thank my family and friends for supporting me throughout writing this thesis and my life in general. Special thanks to Arne for his massive support during the whole process.

Table of Contents

Motivation and objectives

Light-sheet microscopy is a technique that has proven to be an outstanding technology for high content, high-speed imaging of intact living specimens [1–3]. In the last years, a lot of effort was put into making light-sheet microscopes deliver higher axial resolution and time resolution. In the case of axial resolution, many efforts were directed into shaping the beam with which the sheet is created, knowing that the thickness of the beam determines the maximum resolution [4–7]. In the case of time resolution, many commercial systems face the constraints of having to perform for a wide variety of applications and therefore cannot put as much emphasis as other custom-made microscopes on acquisition speed.

In this context, the objectives of this thesis are:

1. To assess the influence of light-sheet thickness on image quality parameters like resolution and contrast, and to carry out a systematic comparison of the performance of various light-sheet modalities found in literature in terms of their light-sheet thickness.
2. To develop a modular solution to increase the acquisition speed in a commercial light-sheet microscope, the Leica TCS SP8 DLS.

The outcomes of pursuing these two objectives comprise this thesis, divided into three chapters. In Chapter 1, as an introduction, the state of the art in light-sheet microscopy is reviewed, as well as the main concepts regarding image formation and image quality. In Chapter 2, the main concepts necessary to assess axial resolution and contrast are introduced and o assess the influence of light-sheet thickness on image quality parameters as resolution and contrast, and to present a systematic comparison of the performance of various light-sheet modalities found in literature in terms of their light-sheet thickness. In Chapter 3, the different aspects to be taken into account when imaging at high speeds are discussed. Special emphasis is put on noise and the choice of camera sensors. Finally, in this same chapter, the modular solution developed to increase the acquisition speed in a Leica TCS SP8 DLS is presented and some examples of its possible uses are showcased.

Resumé étendu en français

La microscopie à feuilles légères est une technique qui s'est avérée être une technologie exceptionnelle pour l'imagerie à haute vitesse de contenu des spécimens vivants intactes. Au cours des dernières années, beaucoup d'efforts ont été déployés pour faire en sorte que les microscopes à feuilles légères offrent une résolution axiale plus élevée et la résolution temporelle. Dans le cas de la résolution axiale, de nombreux efforts ont été dirigés vers la mise en forme du faisceau avec lequel la feuille est créée, sachant que l'épaisseur du façade détermine la résolution maximale. Dans le cas de la résolution du temps, de nombreux systèmes commerciaux font face aux contraintes de devoir exécuter pour une grande variété d'applications et ne peuvent donc pas mettre autant d'accent que d'autres microscopes personnalisés sur la vitesse d'acquisition.

Dans ce contexte, les objectifs de cette thèse sont :

1. Évaluer l'influence de l'épaisseur de la feuille sur les paramètres de qualité d'image tels que la résolution et le contraste, et effectuer une comparaison systématique des performances des différentes modalités de feuille de lumière trouvées dans la littérature en termes de leur épaisseur.

2. Pour développer une solution modulaire pour accroître la vitesse d'acquisition dans un microscope à feuilles légères commercial, le Leica TCS SP8 DLS.

Les résultats de la poursuite de ces deux objectifs comprennent cette thèse, divisée en trois chapitres. Dans le chapitre 1, comme introduction, l'état de l'art de la microscopie à feuille de lumière est examiné, ainsi que les principaux concepts concernant la formation d'image et la qualité d'image. Dans le chapitre 2, les principaux concepts nécessaires pour évaluer la résolution axiale et le contraste sont introduits et l'évaluation de l'influence de la épaisseur de

la feuille lumineuse sur les paramètres de qualité d'image tels que résolution et contraste, et de présenter une comparaison systématique des performances des différentes modalités de feuilles lumineuses trouvées dans la littérature en termes de leur épaisseur de feuille. Dans le chapitre 3, les différents aspects à prendre en compte lors de l'imagerie à grande vitesse sont discutés. Un accent particulier est mis sur le bruit et le choix des capteurs de caméra. Enfin, dans ce même chapitre, la solution modulaire développée pour augmenter la vitesse d'acquisition dans un Leica TCS SP8 DLS est présentée et quelques exemples de ses utilisations possibles sont présentés.

La microscopie à feuilles légères s'est avérée être une technologie permettant de mener des recherches dans un certain nombre de domaines, y compris la biologie du développement, biologie cellulaire, neuroscience et bien d'autres. Les applications bénéficient de la faible photodamage et d'une grande vitesse d'acquisition d'images grâce à une utilisation efficace de la lumière et à un haut degré de parallélisation. Le but de la feuille de lumière est de trancher de manière optique l'échantillon pour générer des images avec un contraste élevé des échantillons fluorescents épais. L'épaisseur de la tranche dépend de l'épais de la feuille de lumière. En d'autres termes, la feuille de lumière détermine complètement la section optique. L'éclairage par une feuille de lumière plus épaisse entraîne la projection d'une section plus épais de l'échantillon en une seule image. Si la feuille lumineuse est plus épaisse que la profondeur de mise au point de la lentille de détection, le contraste de l'image diminue en raison d'informations floues provenant des régions d'objets éclairées par la feuilles lumineuses mais en dehors de la focalisation de la vitre. Dans les échantillons tridimensionnels fluorescents épais, la section optique (OS) est nécessaire pour générer un contraste d'image. Étant donné que la résolution dépend du contraste, c'est-à-dire que la séparation des caractéristiques individuelles n'est possible que pour une baisse suffisante du signal entre deux caractères, la section optique doit être considérée comme l'un des paramètres fondamentaux d'un microscope à feuilles lumineuses. La longueur de la feuille détermine le champ de vision qui peut être illuminé uniformément – avec une section optique et une résolution axiale presque égales. En raison de la diffraction, l'épaisseur dépend de la longueur de la feuille de lumière: Une feuille conventionnelle de faisceau de Gauss créée à une NA plus élevée est plus fine à sa taille, mais la distance au-dessus de laquelle elle reste mince est également plus courte. Dans les microscopes couramment utilisés qui illuminent et détectent la lumière en utilisant une seule résolution objective est anisotrope. Dans un microscope à feuille de lumière, la résolution latérale est déterminée par la NA de l'objectif de détection seule et la résolution axiale est également influencée par le profil d'intensité de la feuille de lumière, de l'objectif d'illumination. Une comparaison quantitative de la résolution de la feuille de lumière

Beaucoup de chercheurs ont mis beaucoup d'effort à améliorer les propriétés de la feuille de lumière par son influence sur la qualité de l'image. La feuille statique a été remplacée par une feuille de lumière numérisée et la forme holographique du faisceau a été employée pour générer des faisceaux de Bessel pour réduire les artefacts dispersés construits sur leurs propriétés d'auto-reconstruction. Étant donné que les faisceaux de Bessel ont également été trouvés non diffractants, ce qui signifie que leur profil ne change pas sur des distances significatives, des tentatives ont été entreprises pour les utiliser pour fournir une résolution plus élevée sur des champs de vue plus grands, qui ont nécessité des efforts supplémentaires, tels que l'éclairage structuré ou l'excitation à deux photons, la détection confocale ou l'application du principe STED pour récupérer le contraste de l'image. D'autres feux non diffractants tels que les feux Airy numérisés ou le feux Sectioned Bessel numérisé mais aussi les feuilles Static Line Bessel et des feuilles Airy statiques ont également été employés. La superposition cohérente des faisceaux de Bessel, appelée feuille de lumière de grille, a été rapportée pour être particulièrement bénéfique en fournissant une résolution spatiotemporelle élevée. En résumé, de nombreux types différents de feuilles lumineuses ont été proposés avec des avantages prometteurs, en particulier en termes de qualité d'image réalisable.

Compte tenu de l'abondance des schémas d'éclairage, une mesure générale pour comparer les avantages des méthodes est souhaitable. Jusqu'à présent, les mesures utilisées pour la comparaison diffèrent entre les publications et varient du contraste d'image, ou des mesures de résolution telles que le profil à travers l'image d'une boule ou la fonction de transfert de modulation (MTF). L'absence d'une mesure uniforme ou l'application de mesures utilisées dans d'autres types de microscopes est un problème pour deux raisons: Premièrement, les propriétés des feuilles lumineuses sont très différentes, et certaines mesures ne peuvent pas expliquer ces différences. Un exemple évident concerne le profil d'intensité de certaines feuilles de lumière qui se décomposent de manière monotone tandis que d'autres présentent des lobes latéraux. Deuxièmement, et plus important encore, ces mesures peuvent ne pas être suffisantes pour refléter l'influence des paramètres qui contrôlent le rapport entre la résolution axiale et le contraste d'image qu'elles fournissent. Par exemple, dans un microscope confocal, la résolution axiale et le contraste de l'image sont liés sans équivoque, c'est-à-dire qu'ils ne peuvent pas être influencés indépendamment. Mais dans un microscope à feuilles lumineuses, la feuille lumineuse peut grandement affecter la résolution et le contraste indépendamment. Compte tenu de ce degré supplémentaire de liberté, nous visons à fournir des mesures pour analyser et comparer quantitativement les feuilles lumineuses dans cette publication.

Dans la deuxième partie de ce travail nous établissons un ensemble de mesures polyvalentes et précises qui prennent en compte les propriétés spéciales de la conception de feuilles lumineuses et permettent de quantifier les caractéristiques qui sont directement

pertinentes pour la qualité de l'image: résolution axiale et sectionnement optique. Les mesures ont été appliquées à une sélection de feuilles de lumière différentes. Grâce à cette évaluation complète, nous avons compris les compromis entre les différentes approches d'éclairage. La question à répondre dans ce document n'est pas principalement de savoir quel faisceau est meilleur que l'autre parce que nous avons trouvé une réponse binaire simple inadéquate. Au contraire, cette étude fournit au lecteur des mesures et un cadre appliqué à une comparaison neutre et rigoureuse entre les compromis qui existent entre les différents concepts d'éclairage dans les microscopes à feuilles lumineuses, permettant une décision éclairée. Cet effort est soutenu par le code Matlab que nous fournissons avec cette publication pour que l'utilisateur puisse simuler diverses feuilles existantes ainsi que de nouvelles et les comparer quantitativement les unes aux autres.

Nous appliquons nos mesures à des données simulées de la répartition de l'intensité 3D des différentes feuilles de lumière pour l'excitation linéaire et à deux photons. Le choix dans notre analyse a été fait selon les règles suivantes: Nous avons limité notre analyse aux types de feuilles légères qui dépendent de la NA et jusqu'à un paramètre supplémentaire. Les feux diffèrent dans l'ordre du polynomial qui décrit la phase des feux: une fonction linéaire pour le faisceau de Bessel, la grille de faisceaux de Bessel et le faiseau double, une fonction carré pour le plate-top focalisé et la faille de Gaussian, une fonction cubique pour la fausse aérienne, et une fonction quarante pour les façades sphériquement aberrées. Des feuilles lumineuses peuvent être générées avec ces faisceaux soit en scannant à travers le champ de vision, soit en façonnant le faisceau directement dans une feuille, par exemple par une ouverture de fente dans l'ouverture arrière de l'objectif d'éclairage. La feuille de ligne Bessel est générée comme un faisceau de Bessel mais avec une ouverture de fente couvrant l'anneau dans le plan focal arrière. En principe, les feuilles de grille peuvent être générées par une structure périodique de fentes dans le plan focal arrière pour n'importe quel type de faisceau, pas seulement le faisceaux de Bessel. Lorsqu'il est formé dans une feuille par une ouverture de fente dans le plan focal arrière, le profil du double faisceau, le Faisceau de haut plat focalisé, le faiseau gaussien, le feux sphériquement aberré reste non affecté.

La simulation est basée sur l'approche du propagateur scalaire qui considère la lumière monochromatique et cohérente. Le propagateur lui-même représente une solution analytique à l'équation de Helmholtz et n'utilise pas d'approximations. La précision de la simulation a été validée. Nous avons fait en sorte que les effets d'apodisation et de polarisation puissent être négligés pour les feuilles lumineuses.

Nous présentons différents types de feuilles de lumière couramment utilisées et introduisons trois mesures:

Deux pour l'épaisseur et un pour la longueur. Plus important encore, nous utilisons deux mesures distinctes pour quantifier différents aspects liés à l'épaisseur de la feuille lumineuse qui ont des significations différentes pour la performance du microscope. Cette séparation est à la fois nécessaire et appropriée pour caractériser une large gamme de feuilles lumineuses.

Conceptuellement, dans les microscopes à feuilles lumineuses une division en deux grandes catégories est utile:

• Les feux de lobe unique : ces feux peuvent être décrits par un seul paramètre : le NA de mise au point. La feuille de lumière la plus couramment utilisée a un profil gaussien. Le profil d'intensité décline monotoniquement du pic suivant une distribution gaussienne. Le profil de Focused flat-top beams est souvent appelé Airy disk. Il présente un pic fort et des côtés très faibles et le ratio de leurs magnitudes respectives est fixe.

• Les feux multi-lobes : ces feux sont déterminés par deux paramètres : le NA et un deuxième paramètre qui est différent pour chaque feux. Exemples constituent le bâton de Bessel, le Bessel beam lattice, Airy Beams, Beams sphériquement aberrés et le Double Beam. Le profil d'intensité des faisceaux multi-lobes ne se décompose pas monotoniquement avec la distance du lobe principal, mais montre un socket (p. ex. pour les feux sphériques aberrés) ou expose des lobes latéraux ou des feuilles latérales. (e.g. for the other three types). Les lobes latéraux portent une grande proportion de la puissance totale de ces faisceaux.

Les feuilles lumineuses peuvent être formées de manière statique, par exemple par une lentille cylindrique dans le chemin du faisceau, par l'étalonnage de la grille ou par la numérisation du Faisceau dans le plan focal de la lentille de détection.

Le travail présenté dans cette thèse contribue à comprendre l’effet de l’épaisseur de la feuille de lumière et de la géométrie sur la résolution et le contraste des images qui peuvent être obtenues avec elle. Les résultats des simulations de propagation des faisceaux présentés dans cette thèse montrent que, contrairement à ce qui a été affirmé dans certaines publications antérieures, la résolution axiale en feuille de lumière ne peut être améliorée que au détriment de la section optique, et vice versa. En d’autres termes, il y a un compromis inévitable entre la résolution axiale et la section optique dans la feuille lumineuse. Le travail présenté ici vise également à offrir des outils pour décider quelle feuille de feuille est la meilleure en fonction de l'application.

Les simulations présentées ne tiennent cependant pas compte des effets de dispersion

introduits par l'échantillon. La stabilité des différents faisceaux à la propagation diffère, comme cela a été montré dans la littérature. Les faisceaux d'auto-guérison, comme ceux de Bessel et d'Airy, se reconstruisent après avoir rencontré un obstacle. Cette propriété les rend plus appropriés pour l'imagerie à l'intérieur d'échantillons hautement dispersés, car leur forme de faisceau est supposée être plus préservée lors de la propagation au sein de ces échantillons. Dans quelle mesure cela peut affecter la résolution efficace et la section optique reste à analyser et est laissé pour le travail futur.

Le simulateur présenté dans ce travail a été développé pour évaluer la géométrie – en particulier l'épaisseur – des schémas de microscopie fluorescente à feuilles légères trouvés dans la littérature. Il offre également la possibilité de mesurer toute feuille de lumière imaginée par l'utilisateur, tant que les images de l'intensité et de la phase du champ électrique sont fournies. Le logiciel Light Sheet Simulator est disponible à télécharger à https://github.com/remachae/beamsimulator. Le dépôt comprend tous les codes source et un manuel d'utilisation.

Dans la deuxième partie de ce travail, les défis de l'imagerie à grande vitesse sont abordés. En particulier, ce travail se concentre sur le choix des capteurs et des bouchons et leur effet sur le rapport signal/bruit. Les possibilités d'utilisation d'une caméra CMOS à éclairage arrière avec une feuille de lumière de faisceau numérisée sont discutées. En particulier, les possibilités d'intégrer une caméra modeste et peu coûteuse dans un microscope commercial permettent d'accélérer l'acquisition. Le potentiel de la mise en place est montré par différents exemples dans le contexte de l'imagerie cardiovasculaire des embryons de zèbres en développement.

La vitesse d'imagerie pour l'acquisition volumétrique en LSFM est limitée par la nécessité de déplacer physiquement l'échantillon à travers une nappe lumineuse et un plan de détection alignés. Pour surmonter ces limitations, certaines méthodes ont été établies dans lesquelles la feuille de lumière se déplace sur l'échantillon, ce qui permet à l'échantillon de rester stationnaire. Pour ce faire, l'objectif de détection doit être recentré de manière synchrone avec la nappe lumineuse. Il existe quatre possibilités pour ce faire : 1) déplacer l'objectif de détection avec la nappe de lumière, 2) adapter le point focal de l'objectif à distance par un système de relais optique, 3) augmenter la profondeur de champ de l'objectif de détection et 4) utiliser un seul objectif. L'objectif de détection peut être déplacé pour que son plan focal coïncide à tout moment avec la nappe lumineuse.

Dans la microscopie à illumination planaire couplée à un objectif (OCPI), l'objectif et le bras d'illumination sont fixés et déplacés par un moteur piézoélectrique. Des méthodes de

focalisation à distance ont été mises au point pour éviter de déplacer l'objectif de détection. Les lentilles accordables électriquement (ETL) peuvent être utilisées pour ajuster la position du plan imagé en synchronisant la tension appliquée pour déplacer le miroir de balayage et le courant appliqué à l'ETL pour déplacer le foyer. La nappe lumineuse de l'ETL peut atteindre une vitesse d'imagerie de 30 à 100 vol/s. Il est possible d'augmenter la profondeur de champ en augmentant la distance entre l'objectif de détection et la nappe optique.

Dans l'extension de la profondeur de champ assistée par aberration sphérique (SPED), la profondeur de champ de l'objectif de détection est augmentée pour éviter la translation de l'échantillon. Pour ce faire, on insère entre l'échantillon et l'objectif de détection un bloc dont l'indice de réfraction est différent de celui de l'échantillon. Cette méthode présente l'avantage de ne pas devoir refaire la mise au point du plan de détection, mais l'inconvénient de devoir effectuer une déconvolution sur les images. Dans la microscopie à fluorescence à détection d'illumination découplée (DID-LSFM), des techniques de codage du front d'onde sont introduites pour étendre la profondeur de champ de l'objectif de détection. Dans la microscopie à plan oblique (OPM), un seul objectif est utilisé à la fois pour éclairer l'échantillon et pour collecter la fluorescence qui en provient.

La fluorescence générée par cette illumination est recueillie par le même objectif et réimagée sur un plan d'imagerie oblique intermédiaire. Les détails les plus importants de ce texte sont les techniques d'imagerie optique utilisées pour imager les myocytes cardiaques à 21 vol/s. La technique SCAPE (Swept confocally-aligned planar excitation) utilise un miroir galvanométrique pour déplacer la nappe de lumière, remplaçant ainsi le moteur piézoélectrique utilisé dans l'OPM. Cette technique permet d'obtenir des images à des dizaines de volumes par seconde et a été utilisée pour obtenir des images du cerveau de souris éveillées et du cerveau de larves de drosophile se déplaçant librement. La microscopie à champ lumineux (LFM) utilise un réseau de microlentilles à la place du capteur dans le plan de l'image, capturant les rayons du champ lumineux provenant des microlentilles.

Chapter 1. **Light-sheet fluorescence microscopy**

1.1 Basic principle of light-sheet fluorescence microscopy

Light-sheet fluorescence microscopy (LSFM) is a technique that is especially well suited for imaging of fast processes or large samples. Its high optical sectioning ability provides images with high resolution and contrast. In LSFM the images are acquired plane by plane, instead of the point-wise acquisition in other technologies like confocal microscopy, which enables higher image acquisition speeds.

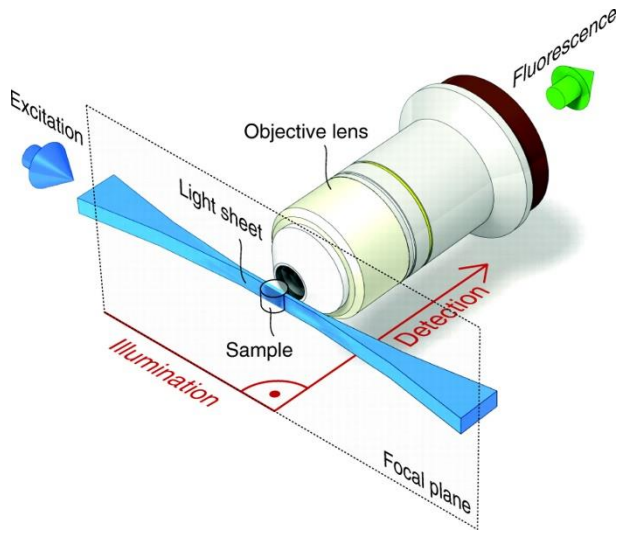

Fig. 1.1 Schematic of a light-sheet microscope setup. A light-sheet is generated that illuminates only the part of the object in the focal plane of the detection objective. Fluorescence light is detected in the orthogonal direction. Figure taken from [2].

In LSFM, a thin sheet of light is generated to excite fluorescence only in a well-defined, thin slice inside the sample. The thin sheet of light can be generated either by using a cylindrical lens or by scanning a beam - generating a virtual sheet of light - which illuminates only the focal plane of the detection optics. The detection system in LSFM generally consists of a widefield microscope with an objective, tube lens, and camera. A schematic is shown in Fig. 1.1. To get a three-dimensional reconstruction of the volume to be imaged, the sample is moved relative to the plane of acquisition, obtaining parallel planar images of the whole volume.

Ideally, the light-sheet has a negligible thickness and is uniform across the field of view; in practice, some limitations occur. There is a physical limit for the thickness of the light sheet since light gets diffracted during transmission through an objective lens. Also, the plane generated is not of uniform thickness but converges to the focus and diverges away from it. To ensure the best resolution, the narrowest region of the light-sheet should coincide with the center of the field of view of the detection system. The thickness of the light-sheet determines the depth of the optical section viewed by the camera and depends on the field of view.

LSFM offers many advantages over other techniques for fluorescence microscopy. First, it provides intrinsic optical sectioning since only a thin slice of the sample receives light excitation. Because no out-of-focus light is created, none is collected. This in turn prevents photo-bleaching outside the plane of interest, a major problem for other established modalities, like confocal microscopy, where the whole sample is illuminated throughout the scanning period for each plane and most of the fluorescence must be rejected and wasted. Here, the confinement of the illumination light to the plane to image ensures that the fluorophores are only excited for the time of exposure of the plane of interest. Optical sectioning, in contrast to physical sectioning, allows the sample to be left intact and alive, a major advantage of LSFM over techniques where samples must be cut before scanning. A final important feature of LSFM is that the wide-field detection provides fast image acquisition, which is not only an obvious advantage by itself, but also allows live imaging of fast dynamic processes.

Heart development has benefited particularly from the capabilities of light-sheet microscopy. In particular, the zebrafish embryo has been extensively used as a model organism for the study of the heart, since the organ is almost transparent, well accessible to the light path, and relatively small [3,8]. With two-photon light-sheet [9], the depth at which the heart can be reconstructed is increased [10,11]. Additionally, other types of samples like spheroids or organoids, which can be too big for confocal microscopes, are still small enough and transparent to be successfully imaged with a standard light-sheet configuration. Organoids can be embedded in hydrogel cylinders, and different fluorescent reporters or even calcium dynamics and cell death can be visualized [12].

Due to the simplicity and potential of light-sheet microscopy, custom-made setups are constantly being published. There exist several open access publications [13–15] that show procedures to build certain light-sheet microscopes. The variety of custom systems allows higher control over image acquisition, but it involves a degree of expertise that may not be accessible to many experimental biology labs. In the following, some of the main light-sheet schemes are presented.

1.2 Light-sheet schemes

1.2.1 Selective plane illumination microscopy and digitally scanned laser light-sheet fluorescence microscopy

Light-sheet imaging was first used in biology to image the beating heart of medaka embryos, as well as the early embryonic development of Drosophila [1] and zebrafish [16]. In the first configurations, light-sheet microscopy was generated using a cylindrical lens to form a static light sheet. This sheet illuminates a thin volume inside the specimen. This technique was called selective plane illumination microscopy (SPIM) [1]. Some years later, a new configuration of light-sheet microscopy was established where a laser beam is scanned to produce the light sheet, which was termed digitally scanned laser light-sheet fluorescence microscopy (DSLM) [16]. Both techniques present some advantages and disadvantages: the static light sheet minimizes laser power density, which is especially desirable to image sensitive live specimens. On the other hand, static light sheets often provide images with striping/shadowing artifacts [17], as a result of the interference produced by perturbations in the light sheet from the sample. In DSLM the artifacts are alleviated due to the spatially incoherent illumination. Another great impact of the introduction of DSLM is that it permitted the development of innovative types of light-sheet microscopy based on beam shaping, structured illumination, and multiphoton illumination [4–6,11,18,19]. The difference between SPIM and DLSM is shown in Fig. 1.2.

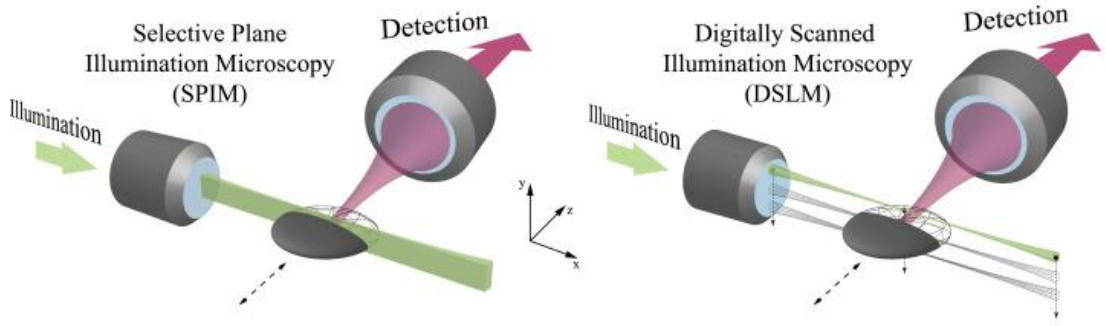

Fig. 1.2 SPIM excites with a thin sheet of light generated using a cylindrical lens located at the back focal plane of the objective lens. In DSLM, a gaussian beam is swept at high speed along the detection focal plane to generate a virtual light sheet. Figure taken from [20]

1.2.2 Multidirectional and multiview light-sheet microscopy

To address the issue of absorption and scattering artifacts, multidirectional selective plane illumination microscopy (mSPIM) was developed [21]. In mSPIM, the light sheet is pivoted, which reduces the shadowing in the sample due to absorption.

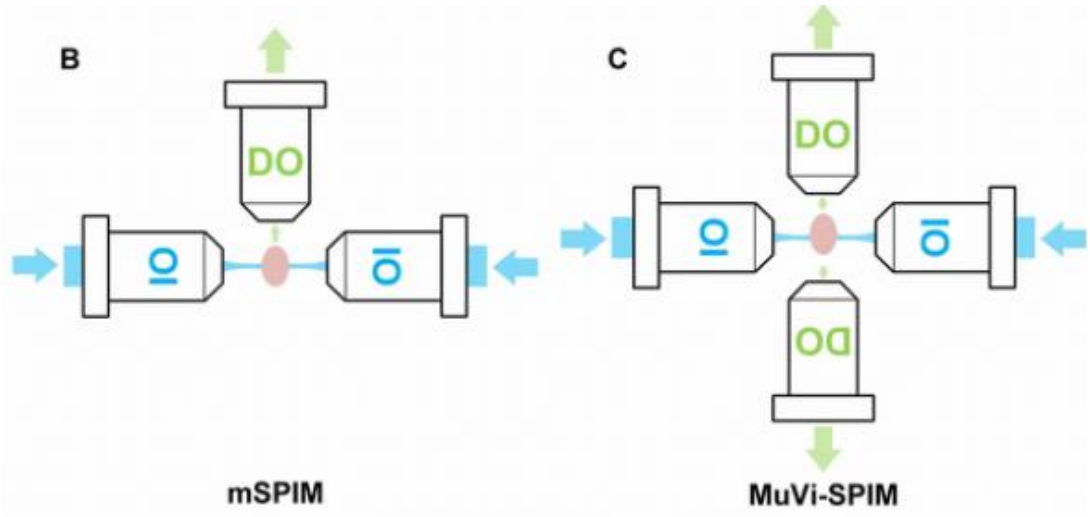

Fig. 1.3 Schemes of (b) mSPIM and (c) MuviSPIM. Figure adapted from [22].

Multiview SPIM or MuVi-SPIM [23] makes use of two sets of orthogonal objectives. Images at acquired at two different views and subsequently merged to increase axial resolution and attain almost isotropic resolution. The main drawbacks of this technique rise from the fact that two full images (one for each objective) need to be acquired: the extra exposure of the sample increases photobleaching effects, and the speed of acquisition is halved. Additionally, the computation of the merged views requires post-processing that may take several hours for large data sets [24,25]. Fig. 1.3 shows the schematics of both mSPIM and MuVi-SPIM.

1.2.3 Enabling horizontal mounting

The configurations described above rely on the mounting of samples in vertical, hanging into a chamber where the objectives, placed in the horizontal plane. Alternatives to these configurations are inverted SPIM (iSPIM) [26]. In iSPIM, the sample is placed horizontally, as in other conventional optical microscopes. The emission and excitation objectives are placed from the top of the sample, perpendicular to each other (see Fig. 1.4). The optics are translated vertically to acquire images at different depths within the sample. With this technique, C. elegans neurons have been imaged and the axon growth and neuron migration could be followed [26].

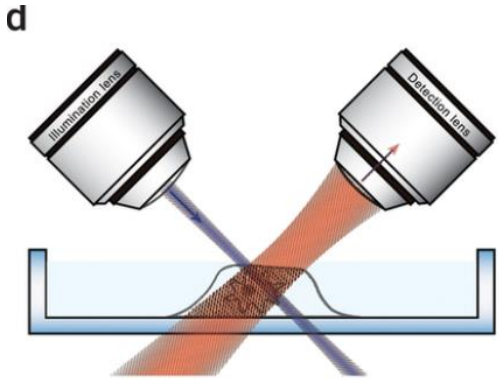

Fig. 1.4 Optical architecture of iSPIM. Figure modified from [27]

Open-top SPIM [28,29], shown in Fig. 1.5, follows a similar approach as iSPIM. In this case, the objectives are located from the bottom of the sample. Between the objectives and the sample, a refractive prism is placed to mitigate the refractive index mismatch between the media and the air. Imaging from underneath allows using more of the working distance of the objective than using the iSPIM setup.

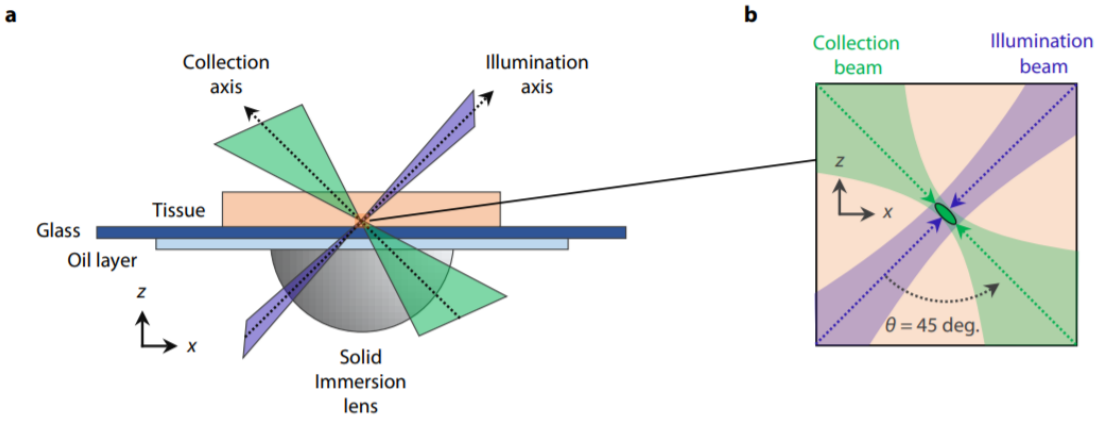

Fig. 1.5 Geometry of open-top microscope. An illumination light sheet enters the bottom surface of a tissue sample at an oblique 45° angle (purple). Fluorescence emission (green), which is generated along the light sheet, is collected in the orthogonal direction by an objective lens. Figure modified from [28]

The geometries used for orthogonal excitation physically limit the maximum usable detection objective numerical aperture. In tilted light-sheet techniques [30], the illumination plane is not completely orthogonal to the detection objective, which allows for a choice of objectives with higher numerical aperture. This idea is performed in lateral interference tilted excitation LITE microscopy [30], to image mitochondria and the nuclear lamina [31].

1.2.4 Single Objective Light-Sheet Microscopy

Using a single objective for light-sheet generation and fluorescence detection has the potential to make light-sheet fluorescence microscopy easier to use and suitable for imaging of large samples and volumetric imaging (Section 3.1.4).

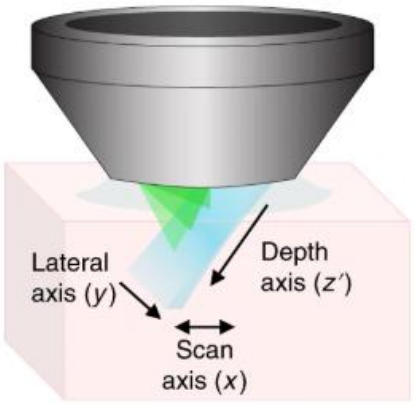

Fig. 1.6 The SCAPE imaging geometry at the sample: an oblique light sheet illuminates the sample along yz', while fluorescence light generated is detected back through the same objective lens. Galvanometer mirror scanning translates both the light sheet and detection plane along x. Figure modified from [32].

Oblique plane microscopy (OPM) [33,34] and swept confocally-aligned planar excitation (SCAPE) microscopy [32,35] employ a single objective of high numerical aperture for both illumination and detection (see Fig. 1.6 for a schematic representation of the principle). The light sheet excites the sample at an angle, which is selected by a mirror. The image from the tilted plane then refocused into a digital camera. The use of a single objective for detection as well as illumination is effective for fast volumetric imaging of small samples such as developing embryos, acquiring full volumes of living samples at speeds in the order of 20 volumes per second [32].

1.2.5 Swept high numerical aperture beams

In axially swept light-sheet microscopy (ASLM), a narrow light-sheet is swept along its propagation path with a remote focusing scan mechanism, and only the in-focus region is imaged [36], as shown in Fig. 1.7. This technique has been successfully used to image migrating cells in complex three-dimensional microenvironments. An alternative to this is diagonally swept light-sheet microscopy (DiaSLM) [37], where they translate the light sheet along a plane at 45° relative to the optical axes, where they place the coverslip of the specimen. DiaSLM was applied to 3D live-cell imaging in different 2D substrates.

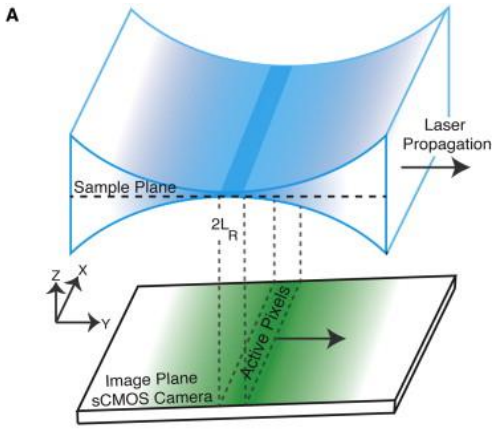

Fig. 1.7 Optical principle of ASLM. (A) The sample is illuminated with a laser propagating along the Y-direction, which is focused to a diffraction-limited line, and fluorescence is collected orthogonally on a camera. Only the pixels that image the beam waist are active. LR is the Rayleigh length of the beam. The axial position of the illumination beam is swept in the Y-direction synchronously with a 2D array of active pixels to generate a large FOV image with beam-waist limited axial resolution. Figure modified from [36].

Combining scanned light-sheet fluorescence and a confocal slit in the detection side, contrast can be improved. Synchronizing the "rolling shutter" with the scanned illumination beam results in confocal line detection [36].

In this thesis I use DSLM. In Chapter 2, I compare the performance of different light-sheet schemes that make use of the beam shaping capabilities of DSLM to try to improve axial resolution. In Chapter 3, I present a modular solution built on a commercial light-sheet microscope that uses a scanned light-sheet.

1.3 The point-spread function

In all types of fluorescence microscopy, the fluorescent molecules can be thought of as point sources of light. The photons emitted by these point sources are collected by the detection objective and finally received by the detector unit. On its way to the detector, the light gets diffracted by the optical components of the microscope. Due to diffraction, the light coming from a point source is not imaged as a point but as a regularly spaced ring-like pattern with local maxima and minima, called Airy disk or pattern, as shown in Fig. 1.8. The size of the central circle in the Airy pattern is defined by the wavelength of light and the aperture angle of the objective. The aperture angle is described by a dimensionless number called numerical aperture (NA) as:

$$\mathrm{NA} = n \sin \alpha \qquad \text{Eq. 1.1}$$

where α is the half-angle over which the objective can gather light from the specimen and n is the refractive index of the imaging medium (normally air, water, oil, or glycerine).

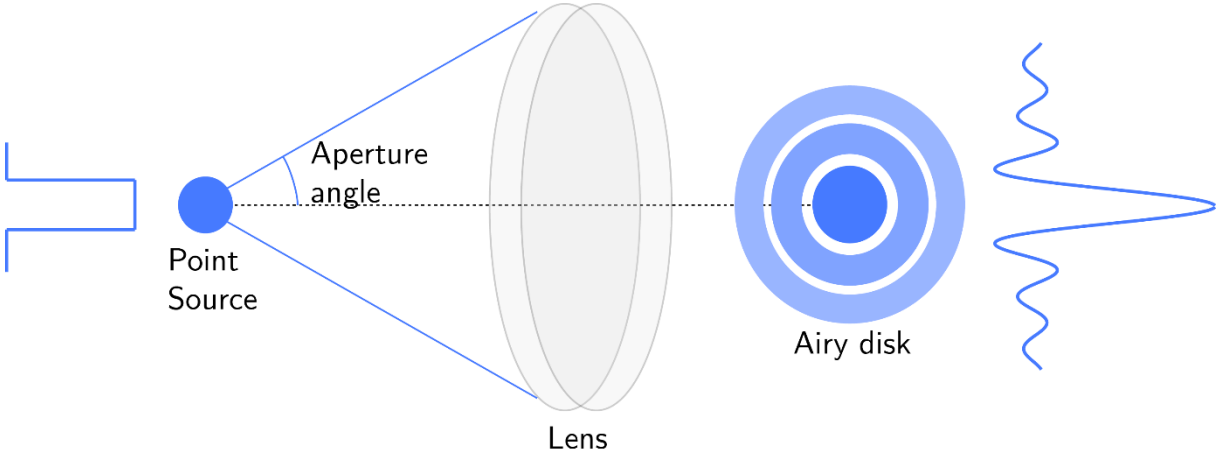

Fig. 1.8 Light emitted by a point source is diffracted by a lens and appears as a ring-like pattern called Airy disk. The half-angle α and immersion medium n determine the number of photons that the optical system can collect and define the numerical aperture (NA). NA is a dimensionless number that determines the performance of the objective.

The point-spread function (PSF) represents the three-dimensional image of a point source object under the microscope. The shape is determined by the optical components of the microscope, the medium where the sample is embedded, and the sample to be imaged, and its extension in all dimensions determines the maximum resolving power of the system.

The first definition for resolution was proposed by Ernst Abbe in 1873 as the minimal distance between two objects that can still be distinguished as individual entities. It is given by the relation:

$$r = \frac{\lambda}{2\mathrm{NA}} \qquad \text{Eq. 1.2}$$

Resolution can also be defined according to the Rayleigh criterion: two point-images are optically resolved if the maximum of the diffraction pattern of one point source coincided with the first minimum of the diffraction pattern of the second. That is, the central region of one Airy pattern overlaps with the first minimum of another Airy disk. If the distance between the two Airy disks is greater than this value, the two objects can be resolved. If the contrary happens, the Airy disks would combine and are considered not to be resolved (see Fig. 1.9).

$$r = 0.61\frac{\lambda}{\mathrm{NA}} \qquad \text{Eq. 1.3}$$

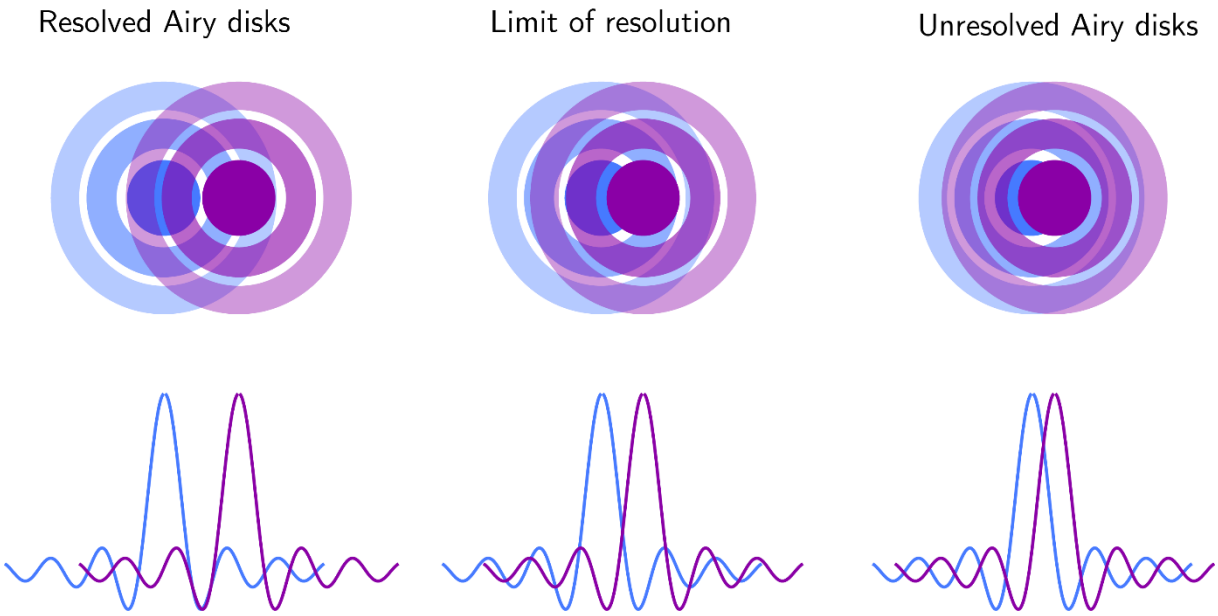

Fig. 1.9 Rayleigh criterion to determine resolution. Two points are resolved if the center of its refraction pattern overlaps with the first minimum of the other one. This happens when their distance is greater or equal than $r = 0.61\frac{\lambda}{\mathrm{NA}}$. If their distance is smaller to this values, the two points cannot be resolved.

As can be derived from this relationship, the resolution power improves with decreasing wavelength and increasing NA. As shown in Fig. 1.10, lower numerical aperture yields larger diffraction patterns or Airy disks, which makes it less likely for two objects placed near each other to be resolved.

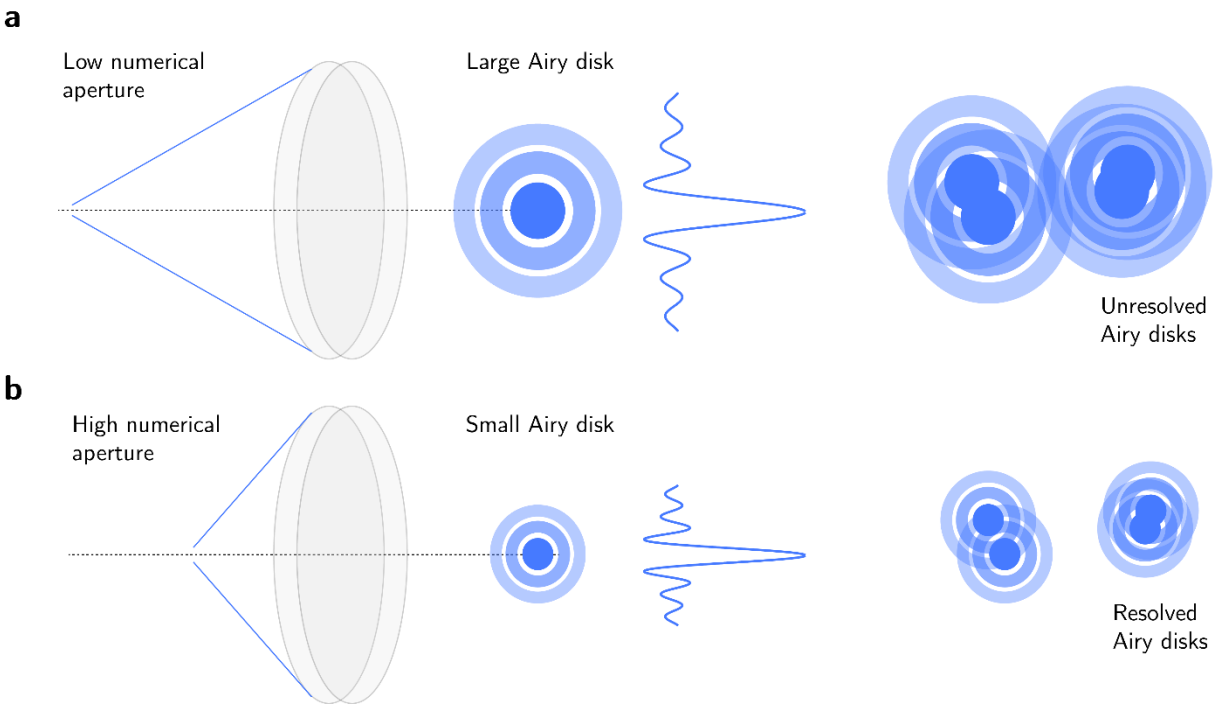

Fig. 1.10 Numerical aperture determines the resolving power of a lens. (a) Low NA leads to greater diffraction patterns, which are more likely to overlap than those resulting from high NA (b). Point sources are therefore more easily resolved with high NA lenses.

1.4 Image formation

The image formation in LSFM can be modeled as:

$$I(x,y,z) = O(x,y,z) * h_{\text{sys}}(x,y,z) \qquad \text{Eq. 1.4}$$

Where $I(x,y,z)$ is the image, $O(x,y,z)$ is the distribution of fluorophores within the sample, and $h_{\text{sys}}(x,y,z)$ is the intensity PSF of the microscope. The intensity of the PSF h_{LS} can be in turn calculated as the product of the illumination and detection PSFs.

$$h_{\text{sys}}(x,y,z) = h_{\text{ill}} \cdot h_{\text{det}} \qquad \text{Eq. 1.5}$$

Both of the intensity PSFs h can be determined from the electrical field H as $h = |H|^2$. The propagated field H after the objective can be expressed as the 2D Fourier transform $\mathcal{F}(x,z)$ of the pupil function $P(k_x,k_z)$).

$$H = \mathcal{F}(P(k_x,k_z)) \qquad \text{Eq. 1.6}$$

The complex pupil function can be written using two real functions:

$$P(k_x,k_y) = A(k_x,k_y)\exp(i\theta(k_x,k_y)) \qquad \text{Eq. 1.7}$$

Where $A(k_x,k_y)$ is the amplitude of the light wave at the entrance pupil of the lens, and $\theta(k_x,k_y)$ is the phase of the light wave.

1.5 Light-sheet thickness and contrast

When a three-dimensional sample is viewed through a conventional widefield microscope, the depth of field of the microscope (that is, the distance between the uppermost and the lowest planes that remain in focus) is normally much longer than the structure of interest. Assuming the typical size of a zebrafish larva heart is about 100 μm, using a typical 20x/0.5 lens, whose depth of field is around 1 μm, approximately only 1% of the light may be coming from in-focus regions. The resulting image is low in contrast, composed of a sharp image of the in-focus region blurred by light emitted or scattered by the tissue above and below the focal region. In

other words, the superposition of the in-focus image with the out-of-focus light reduces the signal-to-background (SBR) ratio, and thus the contrast, of the image. This out-of-focus blur also deteriorates the resolution of detail in the image. The image of the sample would only be completely in focus if the specimen was thinner than the depth of focus of the detection objective. This is usually not the case.

One solution to eliminate the background contribution consists of slicing the specimen into thin sections. This is approach is feasible for fixed samples, but not compatible with imaging of living samples. The alternative approach is to generate an optical instead of a mechanical section through the sample. The parts of the sample that lie in the out of focus regions are reduced and mostly light coming from the in-focus region should be projected onto the sensor. As a consequence, the image has increased contrast, sharpness, and resolution in both the axial and lateral directions.

Optical sectioning is the ability of an optical system to image a thin slice inside a sample. By optically sectioning the sample in thin slices coincident with the focus of the detection objective, the level of background in the image is reduced and the contrast increased. Optical sectioning techniques can produce an image of a plane inside a sample without the need to physically section them. Quantitatively, the optical sectioning (OS) capability is a measure of the contribution of signal from the in-focus plane relative to the out of focus planes. We can calculate the amount of signal detected from each plane z as [7].

$$F(z) = \iint h_{sys}(x, y, z)dx\,dy \qquad \text{Eq. 1.8}$$

Then, for each plane y we calculate the contribution of signal from the focal plane $z = 0$ to z with the integral

$$G(z) = \frac{1}{F_{tot}} \int_0^z F(z')dz' \qquad \text{Eq. 1.9}$$

Where F_{tot} is the total fluorescence detected and can be calculated as $F_{tot} = \int F(z)$. Fig. 1.11 shows a schematic of the calculation of the OS from the illumination PSF.

In a system that offers good optical sectioning, $F(z)$ will be close to a delta function around $z = 0$ and $G(z)$ will have a steep slope around $z = 0$.

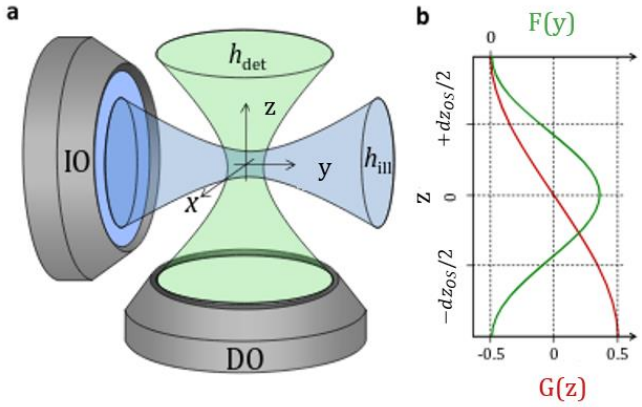

Fig. 1.11 Calculation of the optical sectioning ability from the illumination PSF. Modified from [7].

In this thesis, the optical sectioning will be calculated relative to the illumination PSF, h_{ill}, and not the system PSF, h_{sys}, because the detection optics do not affect optical sectioning by themselves: the integral over the collection efficiency of the signal out of any plane along the optical axis of the detection objective is the same. While collections efficiency from a single point may decrease (i.e. amplitude of h_{sys} decreases) the integral of h_{sys} over the entire plane perpendicular to the optical axis is constant and independent of the distance from the focus. Optical sectioning therefore only arises from light sheet thickness.

Optical sectioning and axial resolution are magnitudes that are related, and both can be obtained from the point spread function. OS, however, gives a more precise measure of the amount of background and contrast in an image.

Contrast, the ratio between the signal and the background, is a key image property because it defines how well information can be extracted from an image. One can have high spatial frequencies and capture small details in an image, but if the amplitude relative to the noise or background is low, it will become hard to recover this. Depending on noise levels it will become hard to extract the resolution if it does not come with enough contrast.

Chapter 2. Thickness and axial resolution in LSFM

Light-sheet microscopy with Gaussian beams presents a fundamental trade-off between the FOV and the light-sheet thickness. Aiming to overcome this, several light-sheet implementations have been published in recent years, using non-Gaussian beams. These include propagation invariant illumination beams, like Bessel and Airy beams, which in theory, maintain a tight 2D focus throughout an infinite propagation length [5,7], and Lattice light-sheet, claiming submicron resolution over big FOV [6,38].

While these techniques have received significant interest, there was a lack of independent investigation and comparison of their optical performance. In this chapter, key optical parameters like resolution and contrast are introduced; a summary of their characteristics and their performance is compared.

2.1 Resolution and field of view

In LSFM, the illumination light is provided by a Gaussian beam, a laser with a Gaussian-shaped intensity profile. In the focal zone, the laser spot exhibits a Gaussian intensity distribution. The shape is shown in Fig2.1. In the plane perpendicular to the optical axis, the intensity profile can be expressed as [39]:

$$i(x,\mathrm{y},z) = i(x,y=0,\mathrm{z})\exp\left[\frac{2y^2}{w(y)^2}\right] \qquad \text{Eq. 2.1}$$

where the beam width $w(y)$ follows the equation of a hyperbole:

$$w(y) = w_0\sqrt{1+\left(\frac{y}{y_\mathrm{R}}\right)^2} \qquad \text{Eq. 2.2}$$

Where $w_0 = \lambda/\pi\mathrm{NA}$ is the beam radius at the waist, $y = 0$, and y_R is the Rayleigh range. The Rayleigh range is the focal region of the beam, that is, the is the region around the waist within which the beam radius is less than $\sqrt{2}\,w_0$.

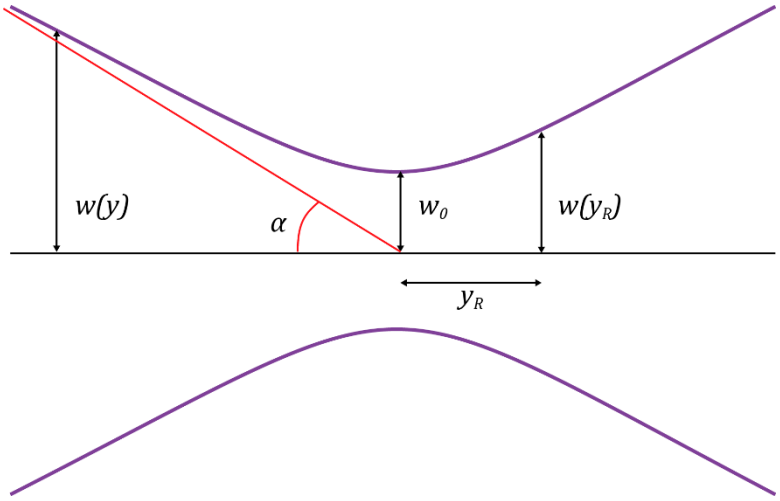

Fig. 2.1 Geometry of a Gaussian beam. Due to diffraction, Gaussian beams converge and diverge from an area of diameter w_0, called the waist. The divergence of the beam is dictated by the divergence angle α, which is defined by the asymptotic variation of the beam radius along the beam direction.

The beam profile diverges away from the focal region. Because of this, there is a compromise between the axial resolution that a light-sheet microscope can provide and the field of view (FOV) that can be imaged, which in turn determines the size of the sample. Far from the waist, the beam diverges with an angle α such that $\mathrm{NA} = n \sin \alpha$. The focal region of the beam, called the Rayleigh range, is the region around the waist within which the beam radius is less than $\sqrt{2}\, w_0$. Hence large NA values yield small waist radii but also a small Rayleigh range.

In LSFM, the lateral resolution is set by the detection objective. The lateral resolution in the focus plane is given by $\mathrm{r_{lat}} \sim \lambda/\mathrm{NA}$. Note, however, that this expression is true only as long as the pixel size of the detection camera remains smaller than $\mathrm{r_{lat}}/2$. In contrast to two-photon and confocal microscopy, in light-sheet microscopy the lateral and axial resolutions are decoupled: the latter is essentially controlled by the thickness of the light sheet, as long as it is not much thicker than the depth of focus of the detection objective. Using a high-NA illumination objective, it is possible to produce a very thin light sheet, whose axial resolution would be greatly improved. However, such configurations have very limited fields of view. Indeed, a very thin Gaussian beam has a small Rayleigh length, i.e. the region over which the beam is highly focused is extremely narrow. As shown in Fig. 2.2, high NA beams are thin and short; low NA beams are thick and long. Nevertheless, these quantities do not vary similarly with increasing NA, since beam diameter scales with $1/\mathrm{NA}$ whereas length scales with $1/\mathrm{NA}^2$.

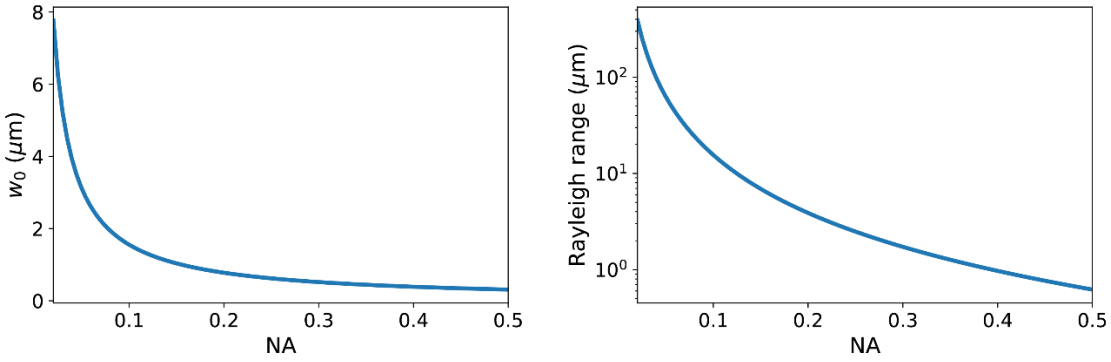

Fig. 2.2 Effect of illumination beam NA on beam diameter and length (measured as Rayleigh range) for Gaussian beams.

In light-sheet microscopy, when using a Gaussian beam for illumination, any configuration bares a trade-off between the axial resolution and the available field of view.

2.2 Beam shaping

To be used for microscopy, Gaussian beams should be shaped to produce the required illumination geometry on the sample. In the most basic implementation of LSFM, the beam is shaped by a cylindrical or a spherical lens to control beam geometry, but there are other means to shape beams.

Beams have been shaped seeking to improve the performance of LSFM at different levels [5–7]: trying to improve the resolution or optical sectioning or increasing the field of view, depending on the particular application and characteristics of the sample. The modification comes usually at the back focal plane of the illumination lens, by shaping the amplitude and or phase of the optical wavefront. It can be achieved by passive optical elements like amplitude masks, phase masks, axicons, etc., or by active elements like spatial light modulators and deformable mirrors. Wavefront engineering can also be done in the detection pathway to increase the depth of focus of the detection lens [40,41]. It should be noted, however, that even though beam shaping can bring advantages to the performance, it comes at the expense of increasing the complexity of the setup and, in some cases, the need for post-processing of the images via deconvolution. In the following, we will analyze the most common implementations of beam shaping to control the light-sheet extent and resolution.

2.2.1 LS formation by a cylindrical lens

The easiest way to generate a sheet of light is by generating a highly elliptical beam by passing a circularly symmetrical beam through a cylindrical lens. This elliptical beam can be modeled as a rectangular slit on the pupil of a spherical lens. The propagation of the resulting diffracted field yields an intensity distribution of a sheet of light.

2.2.2 LS formation by scanned Gaussian beams

Light sheets can also be generated by scanning a focused beam perpendicularly to the detection axis. This is called Digitally scanned laser light-sheet fluorescence microscopy (DSLM) [16].

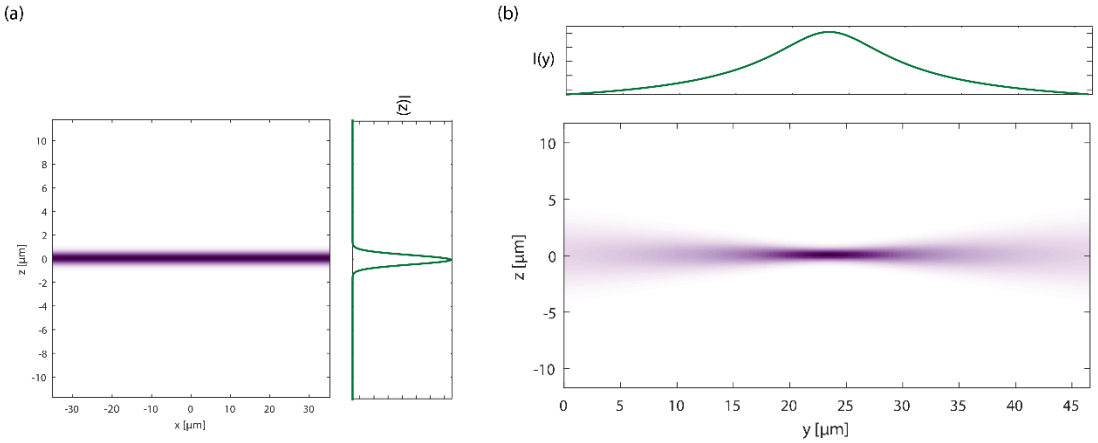

Fig. 2.3 LS generation using Gaussian beams.

The scanning of the beam is possible by introducing a scanning mirror at a plane conjugate to the back focal plane (BFP) of the illumination lens. By scanning the mirror, the beam enters the lens at different angles, which is transformed into a set of parallel beams on the same plane. Integrating the signal over one or more scanning periods, a virtual sheet of light is generated as the summation of the fluorescence at the different beam positions. The shape of these beams can be found in Fig. 2.3, where a cross-section of (a) the scanned beam intensity profile at the focus and (b) the excitation beam are depicted.

Using a scanned beam presents some advantages to using a cylindrical lens. In the first place, the power of the illumination light is contained in a single line, which results in better efficiency. Finally, there is flexibility when deciding the height of the light sheet, since it can be controlled with the amplitude of the scanning. DSLM is less susceptible to scattering artifacts. The disadvantages of this method include that the higher instantaneous intensities of the illumination beam contribute more strongly to phototoxicity and photobleaching.

2.2.3 LS formation by scanned focused flat-top beams

A focused flat-top beam has a uniform intensity profile. Therefore it illuminates homogeneously the back focal plane of the objective lens. The intensity distribution at the focus is described by an Airy disk: it has a main lobe that is surrounded by a dim ring structure. The light-sheet generated after scanning a focused flat-top beam resembles that generated by a Gaussian beam. Its shape is depicted in Fig. 2.4: in (a) the cross-section of the scanned beam

intensity profile at the focus and in (b), a lateral view of the excitation beam. Focused flat-top beams can be used in confocal microscopy to increase lateral resolution because the fluorescence excited by the ring structure is suppressed on the detection side by the pinhole.

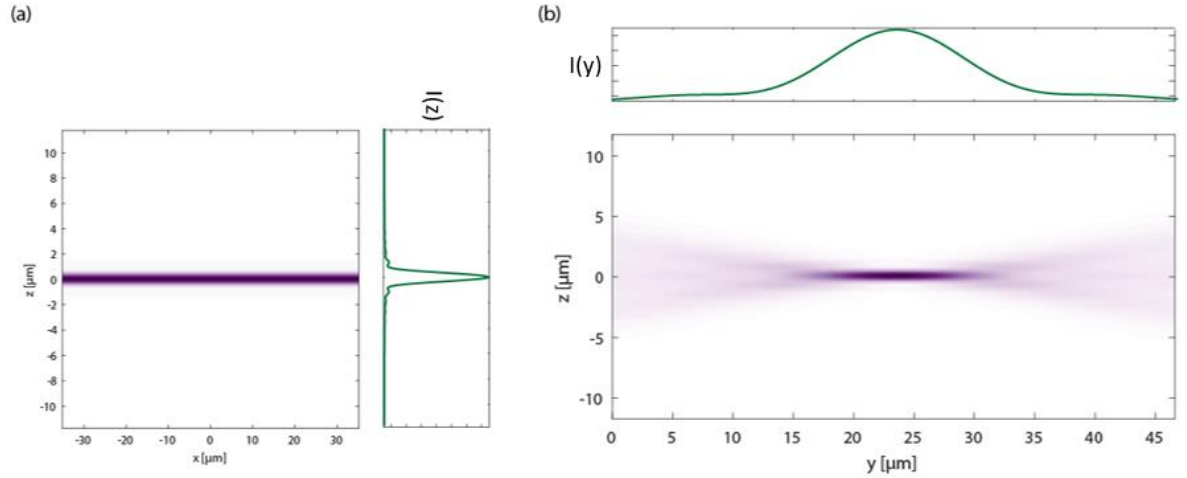

Fig. 2.4 LS generation using Focused flat-top beams.

2.2.4 LS formation by scanned Bessel beams

Efforts to improve the FOV while maintaining high resolution include the use of Bessel Beams for microscopy [7]. Bessel beams are non diffracting beams, that is, they maintain their initial size and shape upon propagation. They have a central lobe which is thinner than those of a Gaussian beam of the same length. However, this lobe is surrounded by a series of concentric rings of light. When scanned, the surrounding rings of light convert into surrounding secondary lobes. The surrounding lobes can be seen in Fig. 2.5, where the cross-section of the scanned beam at the focus is shown in (a), and the lateral view of the scanned beam is shown in (b). Even though the amplitude of the surrounding rings decays rapidly, the energy contained in them does not. The rings contain a large proportion of the beam's total energy.

Bessel beams are produced by creating a set of plane waves whose wavevectors lie on a cone. Since they all have the same radial wave vector, they travel with the same phase velocity and, therefore, the interference pattern never changes. In practice they are created by either of two means: imposing a ring-shaped slit on a laser beam or by using an axicon, a lens with the shape of a cone. In the first case, the annular aperture allows a ring of light to pass, which then is bent inwards by the lens. However, the use of annular apertures is not very efficient, since only a small portion of the light is let through the aperture. In the second case, the axicon bends the incoming light toward the axis, which has the same effect as the annular aperture. In either way, the diffraction pattern that is formed can be described with a Bessel function.

One of the potential advantages of Bessel beams is that the size of the main lobe and the length of the beam can be selected independently. The size and thickness of the annulus can be chosen to select the thickness and length of the resulting beam. Nonetheless, the drawback to increasing the FOV this way is that the light sheet thickens, due to an enlarged size of the ring structure around the central lobe. Therefore, the contrast is lower.

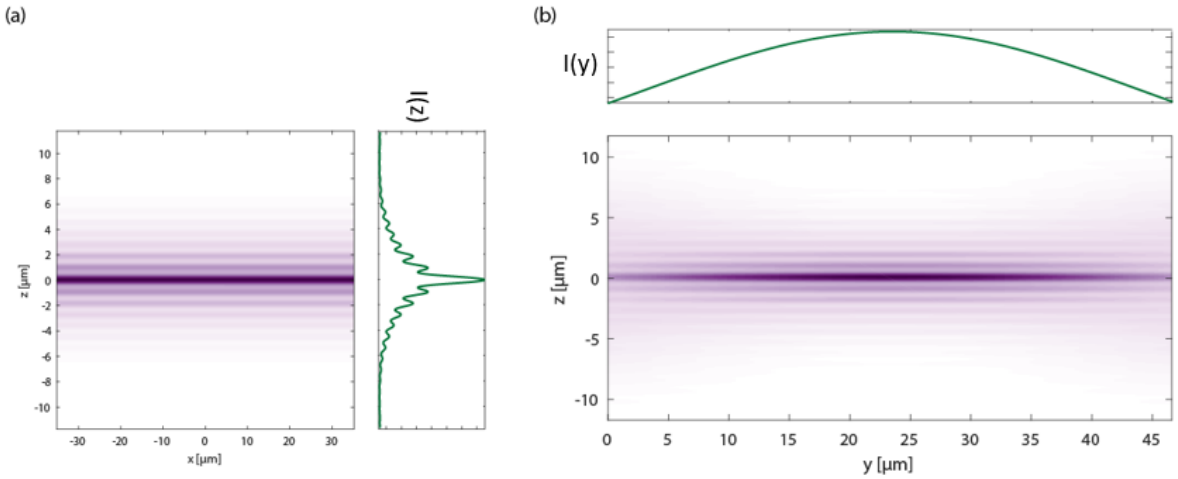

Fig. 2.5 LS generation using Bessel beams.

To avoid these problems and gain contrast and resolution, Bessel beams can be combined with confocal-line detection, structured illumination (SIM), or deconvolution.

Another feature that makes Bessel beams interesting is their self-healing properties: they can recover their shape after being disrupted by an obstacle in the light path. Right behind an obstacle that blocks some of the light, the beam gets disrupted, but upon further propagation, the rays that were not blocked by the obstacle meet again and interfere. Not far from the obstacle, the beam looks the same as before it. This relies on all the rays coming at the same angle with respect to the axis. The self-healing ability is not found exclusively in Bessel beams, but also in other types such as Airy beams.

2.2.5 LS formation by scanned sectioned Bessel beams

The idea behind sectioned Bessel beams is to suppress the side lobes along the detection axis, allowing the Bessel structure along the orthogonal axis. They can be generated by blocking opposite sections of the beam angular spectrum [4]. Ideally, sectioned Bessel beams provide larger FOV than Bessel beams without compromising resolution and contrast. They are aimed at reducing the disadvantageous effects of the side illumination while maintaining the self-reconstruction abilities of Bessel beams. They possess a ring system only in those parts of the

beam not intersecting with the detection cone and therefore excite intrinsically less background fluorescence and generate higher contrast images [4]. The ring structure generates side lobes upon scanning, as in the case of Bessel beams. These side lobes are shown in Fig. 2.6. Sectioned Bessel beams have been proposed for imaging of big samples where scattering was the main issue.

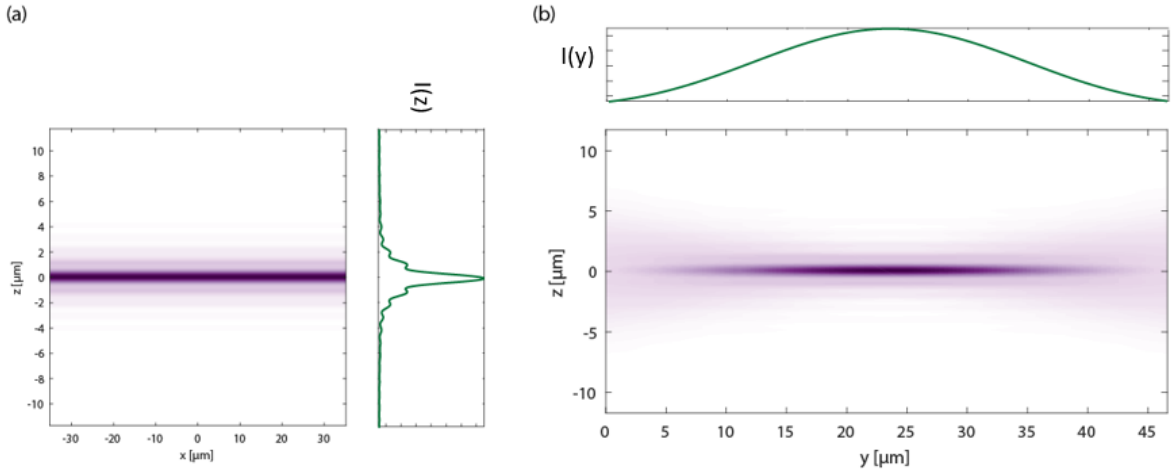

Fig. 2.6 LS generation using sectioned Bessel beams. Cross-section of (a) the scanned beam intensity profile at the focus and (b) the excitation beam.

2.2.6 Lattice light-sheet

In lattice light-sheet microscopy (LLS), a 2D optical lattice is created by superimposing an array of coherent Bessel beams. Depending on the distance at which the beams are separated different interference patterns are created. LLS was reported to provide high spatiotemporal resolution [6], which would make the technique especially suitable for cell imaging. These claims have been questioned in the work presented in this thesis (in section 2.3) and a recent work comparing lattice and Gaussian illumination [42]. The main advantage of Bessel Lattices over other techniques is reduced photobleaching and toxicity. This results from the reduced peak intensity as compared to the use of Gaussian beams.

Two major variants of the technique exist. The hexagonal lattice has a thin beam waist that is surrounded by sidelobes. These sidelobes grow in intensity upon propagation. The square lattice has a thicker beam waist with smaller side lobes surrounding it. Although hexagonal lattice yields better axial resolution, the square lattice is the one that is more used, since it has a better balance between optical sectioning and axial resolution. Bessel lattices can be designed for different purposes. One of the options is meant to increase the axial resolution by using structured illumination microscopy. This is the case for the so-called Hexagonal Lattices. Naturally, the speed of acquisition in this modality is compromised, since, in SI, several images

need to be acquired to obtain one single final image. Scanning this pattern could be used for the generation of LS, but as explained in section 2.3, the additional sheets of light decrease notably the optical sectioning. This is why this configuration is mainly used in SIM. Nevertheless, if SIM is used, deconvolution is required to recover the images.

The other option is by using Square Lattices, which is aimed at increasing the optical sectioning ability of the microscope, maintaining high speed. In the high-speed configuration, the lattice is dithered yielding a series of parallel sheets of light with a homogeneous transversal intensity profile. Their profiles are shown in Fig. 2.7.

In practice, LLS is generated by imposing a set of slit apertures on a ring pupil typical of Bessel Beams. By changing the spacing of the slit apertures, a square or a hexagonal lattice can be generated.

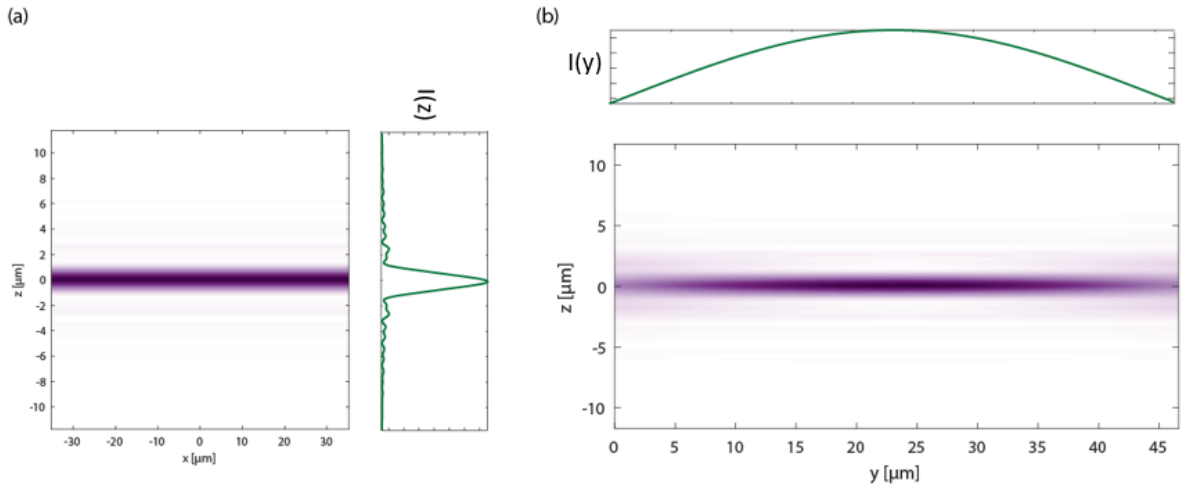

Fig. 2.7 LS generation using a square lattice. Cross-section of (a) the scanned beam intensity profile at the focus and (b) the excitation beam.

Lattice light-sheet can be very sensitive to any perturbation produced by the sample [43]. This may prevent the application of this technology for imaging thick samples.

2.2.7 LS formation by scanned Airy beams

The intensity features of an Airy beam follow a curved parabolic trajectory-in a way analogous to that of a projectile moving under the action of gravity. The main lobe is displaced laterally upon propagation, along a parabolic self-accelerating trajectory, as shown in Fig. 2.8 (b). In the focus, shown in Fig. 2.8 (a), the profile is asymmetric, as side lobes are found on only one side of the main lobe. As Bessel beams, Airy beams exhibit self-healing properties, so they tend to reform or reconstitute themselves after perturbations [5]. Airy beams are generated by imposing a cubic phase mask on the illumination aperture. The phase mask can be generated

by a spatial light modulator or, less commonly, with a tilted cylindrical lens. These characteristics make them more amenable to partially absorbing or scattering samples.

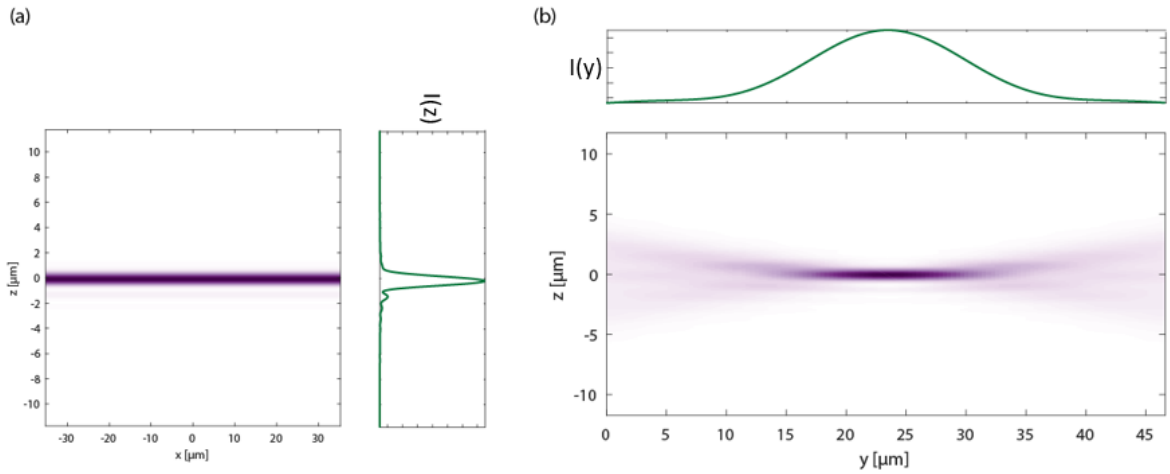

Fig. 2.8 LS generation using Airy beams. Cross-section of (a) the excitation beam and (b) the scanned beam intensity profile at the focus.

A major drawback of LS with Airy beams is that deconvolution is necessary to recover the maximum axial resolution and optical sectioning.

2.3 How to define and optimize axial resolution in light-sheet microscopy: a simulation-based approach

Chapter 3. Implementation of a modular solution for high-speed acquisition on a commercial light-sheet microscope

Light-Sheet microscopy is a particularly fast microscopy technique well-suited for live imaging due to its efficient use of light. Using custom-made systems and fast sCMOS cameras it has recently become possible to image at rates of several 100 frames per second in single planes and with more sophisticated systems to reach volume rates of 10s of volumes per second [32,35]. This level of performance is more challenging to achieve in commercial systems that need to serve a wide range of applications.

In this chapter, a modular solution is introduced to upgrade the Leica TCS SP8 DLS with minimal modifications and optimize it for the highest acquisition speeds. We use a CMOS camera (Baumer VCXU-50M) with a global shutter to avoid image artifacts and overcome limitations due to synchronization issues between the shutter and the scanned illumination beam. The additional camera is synchronized with the microscope by trigger signals but controlled by a simple LabVIEW program on a separate computer to minimize interference with the standard setup. We demonstrate imaging at framerates of up to 600 fps.

3.1 General considerations for imaging of fast-moving objects with LSFM

Many relevant biological processes that occur at the tissue scale, happen in time scales smaller than the microsecond and at three dimensions. Examples of this are the action potentials in the neurons, calcium signaling in the beating heart, or the beating heart itself. It is of crucial importance that the microscopy techniques used to investigate these processes can image this huge diversity of spatial and temporal scales.

3.1.1 Required framerates and artifacts

While imaging fast-moving samples the recorded object may show a spatial distortion because of two facts: sample velocity and readout time. The interpretation of those images with distortions or artifacts can yield misleading conclusions and therefore they must be avoided.

In the previous work from Vermot et al. [44], they revisit the concept of PSF when applied to a moving object. They state that the image of a moving fluorophore is the sum of the images of a static fluorophore at all the positions that it occupies over the integration time. That is, the PSF of a moving fluorophore would be equal to the integration of the PSF of a static one over the trajectory that it follows on the exposure time. If the PSF of an immobile source has the width Δx, the PSF of the moving source with velocity v will be

$$\Delta x' = \Delta x + v\,T \qquad \text{Eq. 3.1}$$

where T is the integration time. The widening of the PSF due to the movement of the light source is depicted in Fig. 3.1.

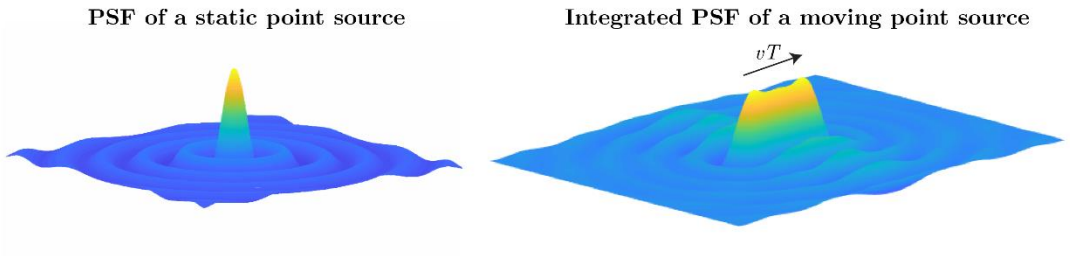

Fig. 3.1 PSF of (a) a static point source and (b) a moving source. When the point source is in motion, its PSF is widened to an extent that depends on the velocity and the integration time.

This widening of the PSF produces a motion blur. Motion blur occurs if the sample moves a significant distance during the exposure time. The amount of blur B that will be present in the image can be modeled as the relative increase area of signal with respect to the size of the original object. This can be expressed as:

$$B = \frac{\Delta x' - \Delta x}{\Delta x} = \frac{v\,T}{\Delta x} \qquad \text{Eq. 3.2}$$

Given a tolerated amount of blur B_0, the maximum exposure time allowed would be:

$$T \leq \frac{B_0\,\Delta x}{v} \qquad \text{Eq. 3.3}$$

For example, an object of 10 µm moving at a velocity of 50 µm/s needs to be recorded with exposure times of at most 20 ms to avoid a 10 % motion blur. However, even if the exposure time is already very small there may still be a distortion for large and fast-moving samples due to rolling shutter.

The third type of artifact present in imaging is temporal aliasing. It occurs even if the exposure time is low enough to capture the sample as a static object, but the time between two acquisitions is too large so that the actual motion is difficult to interpret. It is the case of cyclic or oscillatory motion, where the frequency of the motion can be misinterpreted.

3.1.2 Fluorophores

Imaging at high framerates inevitably implies low exposure times, therefore the time available to collect photons is reduced. The exposure time greatly impacts the signal to noise ratio (SNR) (see section **Error! Reference source not found.**), a key aspect for image quality and computational analysis. Often the limitation for the speed of acquisition is the SNR and not the potential speed microscope. Choosing a fluorophore that allows capturing many photons in a short time is crucial for good image quality at high acquisition speeds. In other words, the brighter a fluorophore, the fewer photons are required to illuminate the sample, which allows for illumination time reduction. The efficiency of fluorescence emission is quantified by the fluorescence quantum yield, defined as the ratio of the number of photons emitted and the number of photons absorbed by the fluorophore. However, for a fluorophore to be bright, it must also have a high capacity to absorb photons, defined by the extinction coefficient. For that, molecular brightness is defined as the product of quantum yield (QY) and extinction coefficient at the excitation wavelength, ε_{exc}. In table Table 3.1 there is a summary of the characteristics of some of the most used fluorescent proteins for live imaging.

Apart from the brightness, we should keep in mind that a suitable fluorophore should be sufficiently photostable and conveniently excitable by the available light sources without producing excessive fluorescence background from the biological matrix (intrinsic fluorescence). In addition to these photophysical properties, basic physical and chemical properties also govern the choice of a particular fluorescence label. Ideally, the excitation wavelength should coincide with the wavelength region that yields the best optical transmission through the sample and minimum autofluorescence. Because phototoxicity and light scattering are reduced at long wavelengths, fluorophores with excitation or emission maxima in the near-infrared (NIR) are offer the advantage of higher penetration depth.

Fluorescent protein	Ex	Em	ε	QY	Brightness
Violet					
Sirius	355	424	15,000	0.24	3600
Blue					
EBFP2	383	448	32,000	0.56	17,920
Azurite	384	450	26,200	0.55	14,410
mTagBFP	399	456	52,000	0.63	32,760
Cyan					
mTurquoise	434	474	30,000	0.84	25,200
ECFP	434	476	32,500	0.40	13,000
Cerulean	433	475	43,000	0.62	26,660
CyPet	435	477	35,000	0.51	17,850
mTFP1	462	492	64,000	0.85	54,400
Green					
EGFP	488	507	56,000	0.60	33,600
Emerald	487	509	57,500	0.68	39,100
mWasabi	493	509	70,000	0.80	56,000
T-Sapphire	399	511	44,000	0.60	26,400
Yellow					
EYFP	514	527	83,400	0.61	50,874
Venus	515	528	92,200	0.57	52,554
Citrine	516	529	77,000	0.76	58,520
YPet	517	530	104,000	0.77	80,080
Orange					
Kusabira Orange2	551	565	63,800	0.62	39,556
mOrange2	549	565	58,000	0.60	34,800
tdTomato	554	581	138,000	0.69	95,220
TagRFP	555	584	100,000	0.48	48,000
Red					
mApple	568	592	75,000	0.49	36,750
mStrawberry	574	596	90,000	0.29	26,100
mCherry	587	610	72,000	0.22	15,840
Far-red					
mKate2	588	633	62,500	0.40	25,000
mPlum	590	649	41,000	0.10	4100

Table 3.1 Molecular brightness, quantum yield QY, extinction coefficient ε_{ex} and excitation and emission maxima for some of the most used fluorescent proteins used in light microscopy. Taken from [45]

3.1.3 Photobleaching and phototoxicity

Increased acquisition speed reduces the exposure time for each frame, the time each fluorophore can be illuminated. To maintain high signal intensity, the strategy could be to increase the illumination power. However, high-intensity illumination increases the risk of photobleaching and phototoxicity.

Upon excitation, a fluorophore might react with molecular oxygen to yield a variety of reactive oxygen species (ROS). Phototoxicity results from the damage caused by those ROS on proteins, nucleic acids, and other biomolecules in the sample. Photobleaching is often caused

by the same process: the generation of ROS due to the reaction between molecular oxygen and the excited dye in the triplet state. The resulting singlet oxygen is highly reactive and may attack a fluorophore and irreversibly impair its fluorescence activity. The process of fluorescence is inherently inefficient, so a high light dose is needed to achieve a detectable emission of fluorescence from the fluorophores. To minimize the light dose, the choice of a bright fluorophore is important (see section 3.1.2).

In LSFM the fluorescence is excited with a light sheet only around the focal plane of the detection objective. Moreover, a 3D stack of images is acquired illuminating each plane only once. Due to this limited illuminated volumes, the energy load on the specimen is reduced compared to other techniques. Therefore, phototoxicity and bleaching are reduced. LSFM is therefore among the most gentle technique for fast or volumetric imaging. The phototoxicity caused by imaging with LSFM has been compared to other techniques in different studies [46–48], where they report better sample health when using the latter.

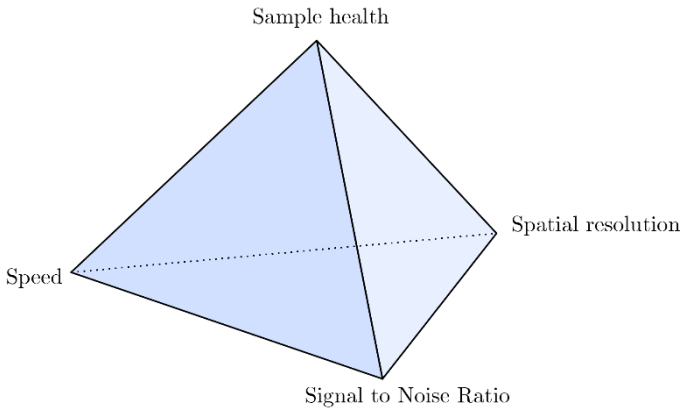

Fig. 3.2 Pyramid of frustration. SNR, spatial resolution, speed, and sample health are interdependent—no single factor can be changed without affecting the others. Optimization of the first three factors often is coupled to increased exposure to light, which usually comes at a cost to sample health.

This interdependence of imaging parameters is represented by the frustration pyramid, shown in Fig. 3.2, which depicts the compromises that must be made in live imaging. To get an image with a high signal, one could be tempted to increase the laser power and acquire for long time windows, but the specimen will likely suffer from high energy exposure. Conversely, exposing for short times and between long time-intervals at low power over will keep the sample healthy, but it may make tracking of your sample difficult.

Regardless of the type of fluorescence microscopy, a simple way to reduce the energy load on the specimen is to minimize overall light exposure. Several studies have been made that show that lowering the illumination intensity [49] or delaying the time between illumination time points [50,51] reduces the effect of phototoxicity and improves sample health. For fast-moving specimens, long exposure times are detrimental since they decrease the maximum

acquisition speed. Additionally, motion blur may appear. However, reducing the intensity and increasing the exposure time is a reasonable recommendation since is very easy to implement without additional hardware.

An alternative, which is more complex and requires hardware modifications, is to pulse the illumination. As opposed to the regular constant illumination of the specimen during the acquisition time, the light is transmitted to the sample in pulses, with breaks between pulses in the range of microseconds. By doing this, one can reduce phototoxicity keeping the peak intensity and overall light exposure. The only difference would be the short additional time of exposure due to the breaks between pulses. To understand how pulsed illumination reduces phototoxicity, first, we should understand the time scales of fluorescence. Fluorescence comprises several phenomena: excitation from the ground state, relaxation through vibration, and returning to the ground state through photon emission. The whole cycle takes around 10 nanoseconds [46]. The excited electrons can, instead of returning to the ground state emitting light, cross to an excited triplet state, where the electrons reside much longer than in the single state. While in the triplet state, an incident photon can induce chemical damage and covalent modifications of excited fluorophores, which are the most normal cause of photobleaching. If instead of constant illumination, we use pulsed illumination, the breaks allow excited fluorophores in the triplet state to return to the ground state, which reduces the rate of destruction of fluorophores. Phototoxicity can also be reduced by implementing pulsed illumination on a point scanning confocal microscope [52]. Moreover, the break between two pulses can give enough time to enable dissipation by heat from the excitation site. In the context of light-sheet microscopy, this could be an argument for using a scanned light-sheet over a static one [53].

3.1.4 LSFM microscopes for high speed and volumetric acquisition

Some phenomena in biology, like the flow of blood cells inside the heart, irregular and non-periodic beats [54], or voltage changes and calcium transients in neuronal networks [55] as well as the dynamics of flow, dilations, and the physical migration of cells through tissues, require a very high volumetric imaging speed of above 50 –100 Hz [56]. Imaging speed for volumetric acquisition is limited in LSFM by the need to physically translate the sample through an aligned light sheet and detection plane. The limitations come from the inertia of the sample and that very high accelerations of the sample could be harmful to the living specimens. To overcome these limitations, some methods have been established in which the light sheet moves across the sample. In this way, the sample can stay stationary. It is important to note that when doing so, the detection objective must be refocused synchronously to the light sheet. There are four possibilities for doing so: 1) moving the detection objective along with the light sheet, 2) adapting the focal point of the lens remotely by an optical relay system, 3) increasing the depth

of focus of the detection objective and 4) using a single objective. They will be explained in more detail in the following and a schematic can be found in Fig. 3.3.

1) Moving the detection objective along with the light sheet.

The detection objective can be translated to make its focal plane coincide with the light sheet at every moment. In objective-coupled planar illumination (OCPI) microscopy, the objective and the illumination arm are attached and translated by a piezoelectric motor [57]. It has been applied in neuroscience to image thousands of neurons simultaneously [58]. In their work, Turaga et al. reveal a new organization model for an entire sensory system, after recording chemosensory responses in the mouse nasal epithelium. Since the detection objective and illumination optics are physically coupled, the volumetric acquisition is performed by moving the parts together along the axis of the objective, instead of moving them independently or moving the sample. On a different setup, a four-objective light sheet microscope, the whole central nervous system of the Drosophila larva was imaged [59]. With it, they could uncover connections between different regions of the nervous system. The main drawback of this technique is, however, the inertia of the objectives and that their movements can induce undesired vibrations in the sample chamber.

2) Remote focusing

To avoid moving the detection objective, remote focusing approaches have been developed. Electrically tunable lenses (ETL) can be used for this purpose [60] and have been used to image the entire beating heart of a zebrafish larva [54]. ETLs are liquid lenses whose focal length can be controlled electronically. Adjusting the focal length of the ETL, the position of the plane that is imaged is fixed. The way to adjust the position is to synchronize the voltage that is applied to move the scanning mirror and the current that is applied at the ETL to move the focus. The tuning makes sure that the image plane and light sheet coincide exactly during the time of the volume scans. The ETL light sheet can achieve an imaging speed of 30 –100 vol/s [56].

3) Increasing the depth of focus

In spherical-aberration-assisted extended depth-of-field (SPED), the depth of focus of the detection objective is increased [40] to avoid translation of the sample. The strategy is to introduce spherical aberrations in the detection path producing a refractive index mismatch. A block of different refractive index to the sample medium is inserted between the sample and the detection objective. The spherical aberrations which extend the PSF and therefore increase the depth of focus. This method has the advantage of not having to refocus the detection plane, but the drawback of having to perform deconvolution on the images, which is computationally expensive. It has been used to image clarified mouse brains and calcium signaling of the

zebrafish nervous systems [40]. A different approach is that of decoupled illumination detection light-sheet fluorescence microscopy (DID-LSFM) [41], where wavefront-coding techniques are introduced to extend the depth of focus of the detection objective. With DID-LSFM, C. elegans has been imaged with speeds of over 70 vol/s [41].

4) Single objective

In oblique plane microscopy (OPM) [33], a single objective is used both to illuminate the sample and to collect the fluorescence coming from it. The sample is illuminated by an oblique light sheet generated with the main objective, and the fluorescence generated by this illumination is collected through the same objective and reimaged to an intermediate oblique imaging plane [61]. The intermediate plane is imaged onto the camera by some additional optics. With this setup, cardiac myocytes have been imaged at 21 vol/s to study calcium dynamics [62]. Swept confocally-aligned planar excitation (SCAPE) uses a galvanometer mirror to move the light sheet, replacing the piezoelectric motor used in OPM. The light coming from the sample is reflected in the same mirror and the light sheet remains in the focus of the camera. This technique enables imaging at tens of volumes per second. It has been used to image the brain of awake mice and the brain of freely moving Drosophila larvae [35]. Another application that this technology enables is the imaging of freely moving specimens, like Drosophila and C. elegans worms [32].

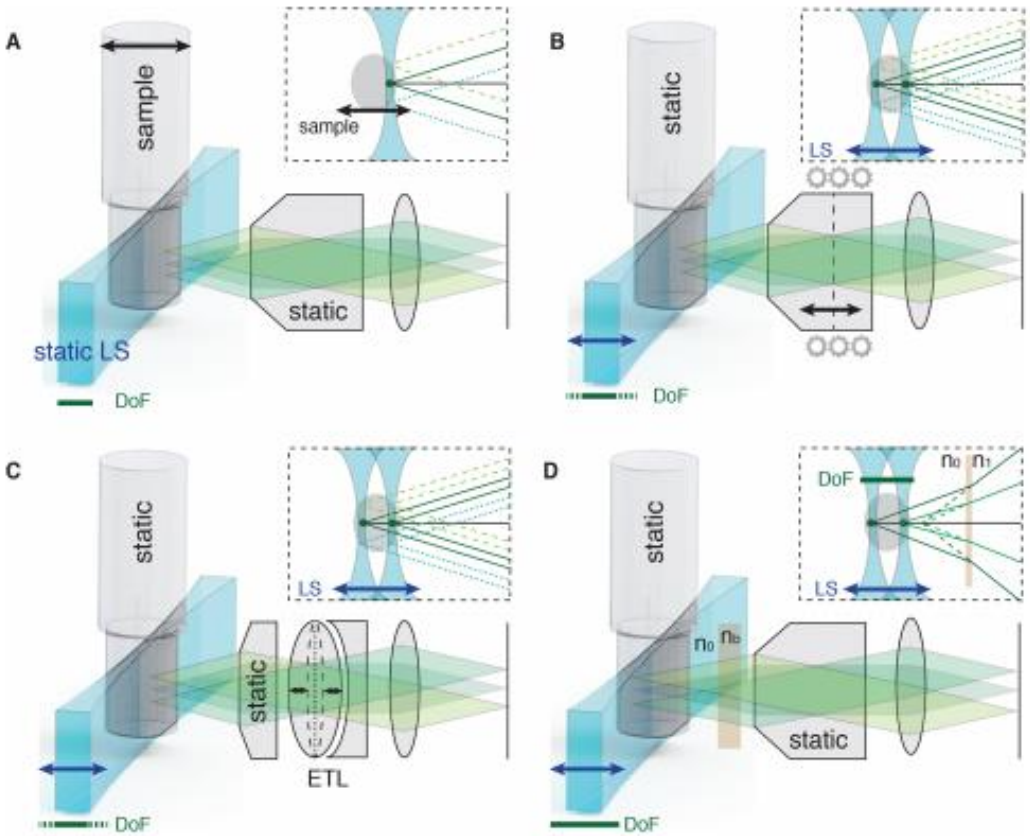

Fig. 3.3 Schemes for fast volumetric imaging in LSFM. Boxes at the top right of each panel represent a close-up view of three selected ray paths between the light sheet and the detection objective. (A) In selective plane illumination microscopy (SPIM), the sample is moved through the static light sheet to generate a 3D dataset. (B–D) In fast volumetric imaging schemes, the light sheet is scanned through the static sample. The shift in the illuminated plane is accounted for by moving the detection objective with piezoelectric translational stages (B) or by remote focusing using an electrically tunable lens (ETL) (C). In contrast, in (D) a plate is inserted that induces spherical aberrations and extends the point spread function (PSF; i.e., close-up view), thus increasing the depth of focus (DoF). For simplification, in the close-up view of (D) only one light path per light sheet is drawn. Green dashed lines indicate the focus of the detection objective without the aberration plate. .Figure taken from [56].

Another optical imaging technique with a high temporal resolution is light field microscopy (LFM) [63]. In LFM an array of microlenses are positioned instead of the sensor in the image plane. The sensor instead captures the light field rays coming from the microlens. With this technique, without the need to scan the sample across the optics, we can obtain information from the location (in 2D) and the angle (in 2D) of the incident light. Reconstructing the images we can obtain a 3D volume and high-speed volumetric acquisition is enabled. This technique has proven its potential by imaging the simultaneous function of neuronal activity in a whole C. elegans and zebrafish larva brain [64]. Nevertheless, LFM is still limited in spatial resolution when compared to LSFM. A similar technique is SVIM [65], a light-field-based selective volume illumination microscopy, where illumination is confined to only the volume of interest, similar to LSFM. This selective illumination helps remove the background. In their paper, they manage to capture the whole beating heart and neuronal activity in zebrafish, as well as flowing bacteria in squid in 3D.

3.2 Choosing the right camera sensor for fast imaging in LSFM

To choose the appropriate camera, we should consider the application we want to use it for. In particular, we care about the intensity of the sample signal in the regions of interest, and the required SNR for the expected analysis. This principle holds regardless of the type of samples to be imaged. Depending on these, we can determine whether camera noise will dominate the regions of interest or shot noise will be the main source of noise.

3.2.1 Camera sensors: CCD, CMOS

Scientific complementary metal-oxide-semiconductor (sCMOS) sensors have gained popularity in microscopy because they offer wider FOV, lower dark noise, and higher frame rates than charge-coupled devices (CCD) [66]. Both sensors work under the principle of collecting a signal charge in each pixel that is proportional to the intensity of the illumination of that pixel. The difference and similarities between them are explained in the following.

Each pixel of a CCD sensor is composed of a photodiode and a potential well. When a photon hits the sensor, the photodiode converts the light into electric charge (photoelectrons). The efficiency of this conversion depends on the wavelength of the incident light and is expressed as quantum efficiency (Qe). Photoelectrons accumulate in the potential wells until readout time, when they are transferred from well to well down each row of pixels. The charge is therefore gathered pixel by pixel, or serially, to a common output structure, where it is converted to a voltage. Since this conversion takes place at a common port, the image acquisition speed is limited. CCDs acquisition speed can be pushed either by reducing the number of pixels per frame to readout, that is, giving up resolution and field of view, or by sacrificing dynamic range and readout noise [67].

Electron multiplying CCDs (EMCCDs) have an extra component that multiplies the photoelectrons generated by the photodiode. The multiplication is done before the readout and with it, the signal of a single photon can be amplified above the readout noise base level [66], even at high acquisition speeds. This characteristic makes EMCCD cameras suitable for imaging with low light conditions. The mechanism needed to perform the multiplication of photoelectron introduces an additional source of noise called multiplicative noise. This can be considered as an increase in the shot noise by a factor of 1.4, which can be also seen as reducing the effective Qe to a half [68].

Unlike CCD (and EMCCD) sensors, each pixel of a complementary metal-oxide-semiconductor (CMOS) sensor is composed of a photodiode and an amplifier. The photoelectrons are converted into a voltage at the photodiode-amplifier pair. Since the conversion happens in parallel, as opposed to serially in CCD and EMCCD, the image acquisition speed can be greatly increased [69]. sCMOS is a technology based on next-generation CMOS sensors that are capable of offering low noise, fast image acquisition, high quantum efficiency, high resolution, and a large FOV [70]. This combination of qualities renders high-speed, high-resolution biological images, even in low light scenarios.

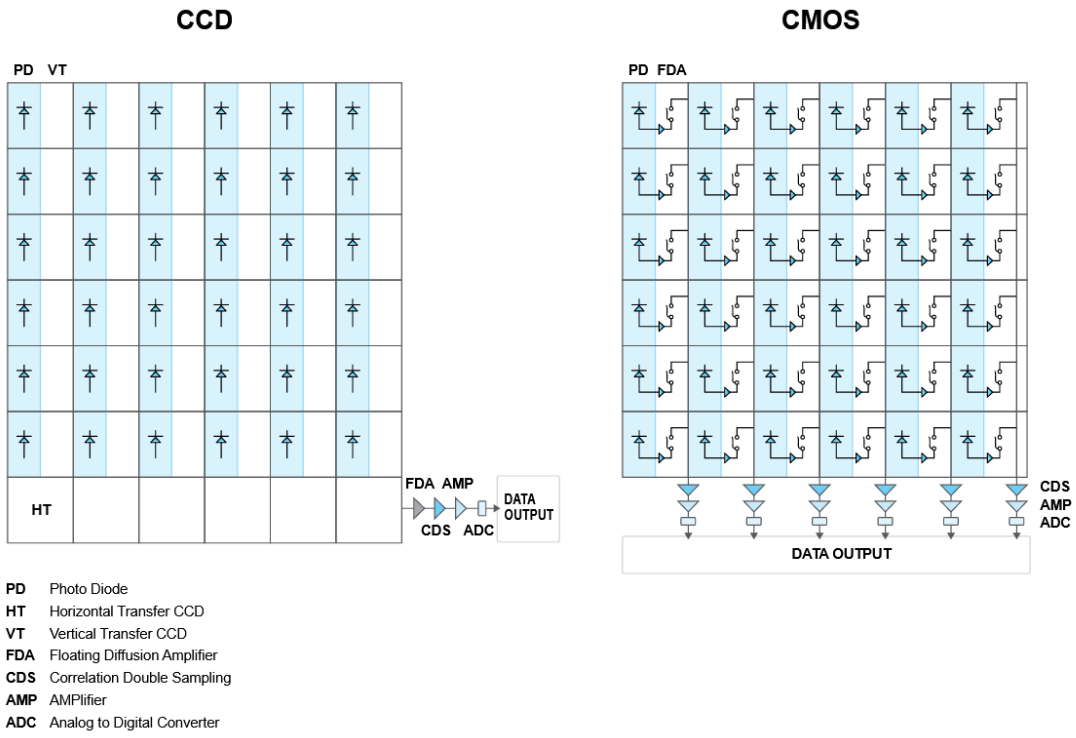

Fig. 3.4 Architecture of CCD and CMOS sensors. Each pixel of the CCD image sensor is composed of a photodiode and a potential well. Light hitting the sensor is converted into electric charge (photoelectrons). Photoelectrons accumulate in each photodiode until it is time for readout when all of the photoelectrons are relayed from one diode to the next down each row of pixels. The charge is gathered serially, pixel-by-pixel, into a container at the end of the relay. Once in the container, the photoelectrons are converted into voltage and processed into an image on the camera circuit board. Because the photoelectrons are converted into the signal at a common port, the speed of image acquisition is limited. In contrast with CCD, each pixel of a CMOS image sensor is composed of a photodiode-amplifier pair. Photoelectrons are converted into a voltage by each pixel's photodiode-amplifier pair. Because voltage conversion happens in parallel instead of serially, as is the case for the CCD sensor, image acquisition can be much faster for CMOS sensors. From Hamamatsu.

3.2.1 Shutters: global and rolling shutter

Until recently CMOS sensors presented mainly rolling shutters, whereas CCD cameras offered global shutters. With a rolling shutter, an image is not illuminated all at once, but rather in a staged sequence. When the shutter release is initiated, the individual lines of the image are exposed one after another, line for line. The difference between global and rolling shutter is shown in Fig. 3.5.

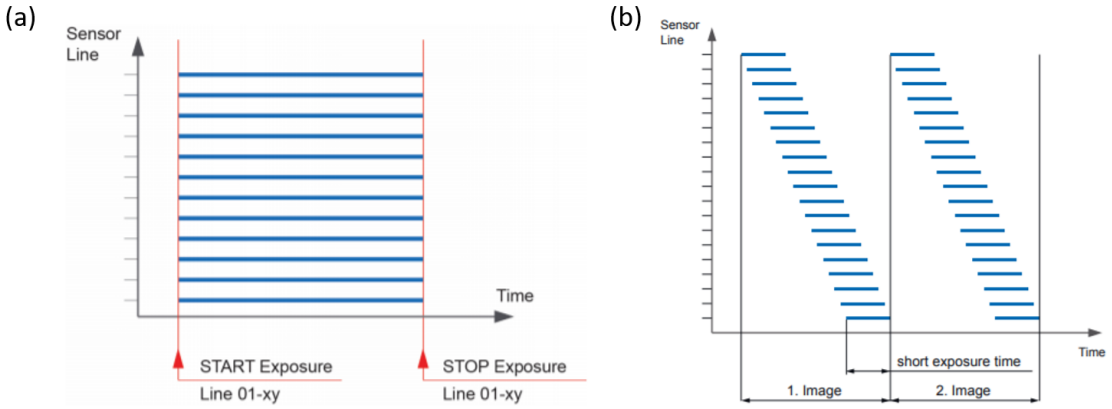

Fig. 3.5 Global vs Rolling Shutter. (a) In a global shutter, the exposure time begins and ends simultaneously for all pixels. (b) For the rolling shutter, the exposure time does not begin and end simultaneously, but rather for each row respectively. From baslerweb.com

The rolling shutter makes many applications in which the examined object or camera moves impossible, since it may result in distortions that will prevent proper image processing. The effect of rolling shutter in the imaging of fast-moving objects can be appreciated in Fig. 3.6, where the rolling shutter effect is depicted for an object moving through the field of view during the acquisition of a single frame. The acquisition time is significantly longer than the exposure time of each pixel row. The camera records a distorted image of the object. For this reason, rolling shutter sensors are not a general recommendation in image acquisition on moving objects.

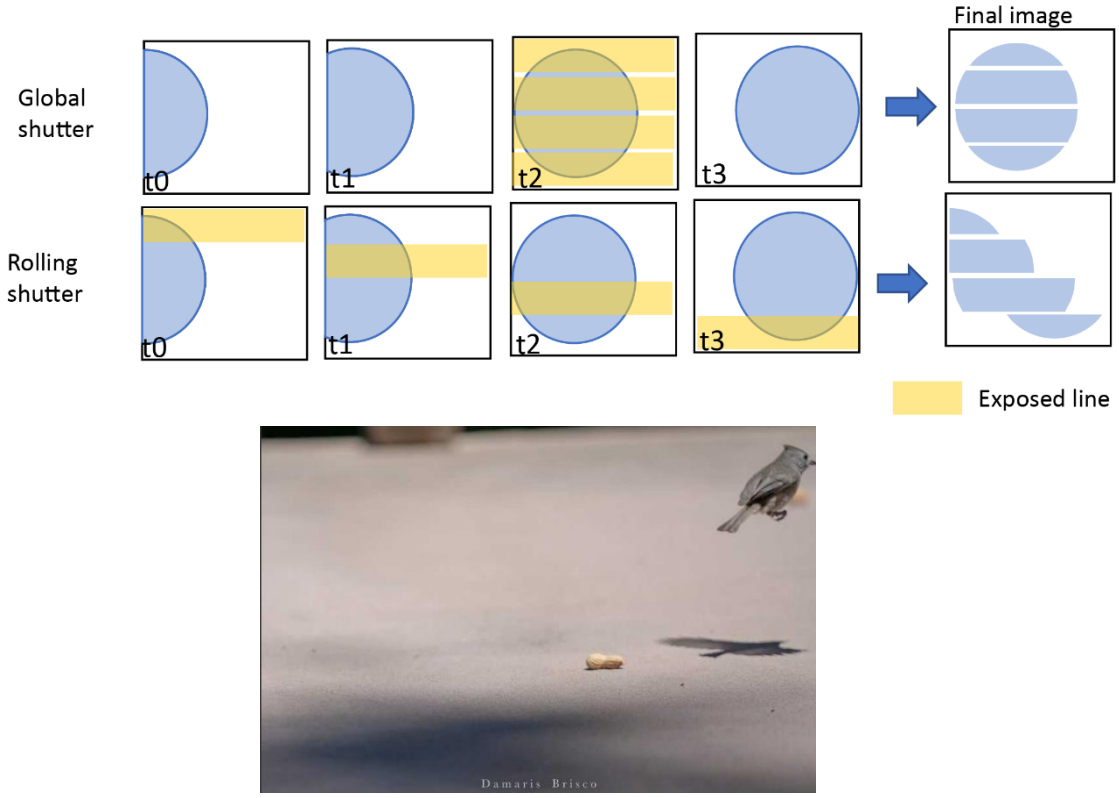

Fig. 3.6 Rolling shutter effect. In rolling shutter cameras, image distortion can occur due to the row by row integration and offset on moving objects. In the picture on the bottom, the effect can be noticed on the difference of position between the bird and its shade.

A way to avoid deformations arising from delayed exposure of different lines, the camera makers usually offer a global exposure mode (see Fig. 3.7). Through global exposure synchronization, rolling shutter cameras can emulate the global shutter CMOS. The exposure time is expanded to allow for a time window when all the pixel rows are being exposed at the same time. This has to incorporate a way to shut off or control the light source. The illumination must be turned on only when all the lines are exposed and turned off during the readout. In this way the sensors can maintain low read noise and dark current, but with a significant time that the sensor is not exposed.

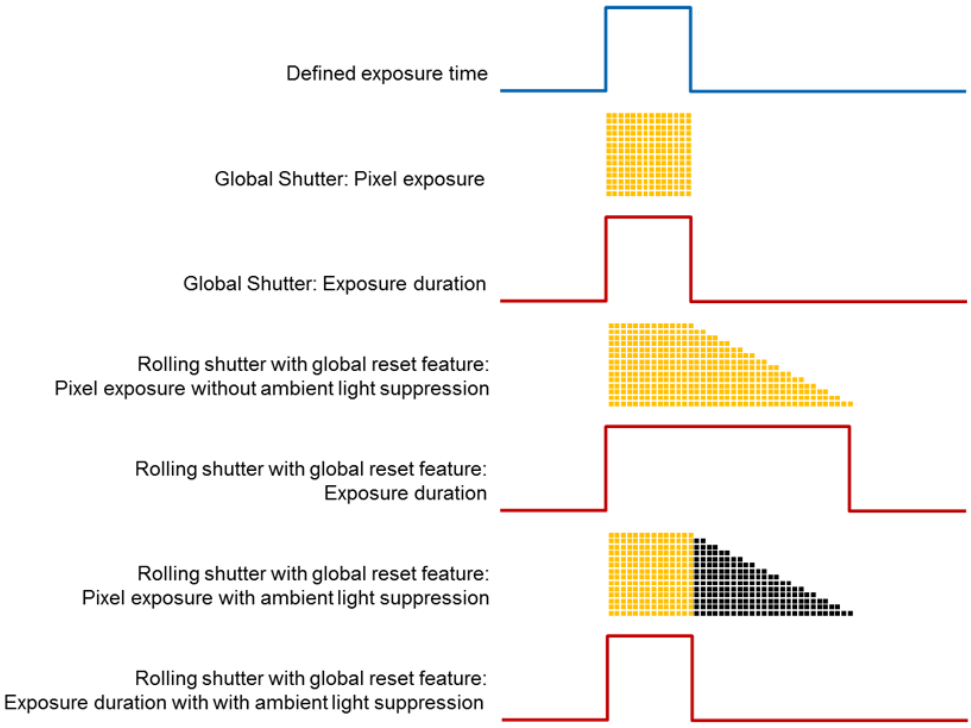

Fig. 3.7 Methods to avoid rolling shutter effect. When using a rolling shutter with global reset mode, all rows start integrating at the same time. A gradient in the image brightness from top to bottom may be seen if ambient light is not suppressed. In the case of ambient light suppression, the exposure of all lines starts and ends at the same time, resembling a global shutter, with the drawback of losing exposure time.

3.2.2 The choice of camera

The camera used in this work uses a new generation of CMOS sensors developed by Sony [71]. They consist of a backside-illuminated stacked sensor that can read every pixel simultaneously to enable a global shutter. Every pixel contains an analog-to-digital converter (ADC) stacked beneath the photosensitive part of the pixel. This allows all exposed pixels to be read simultaneously rather than sequentially row-by-row as is done with traditional CMOS sensors containing far fewer 'column parallel' ADCs.

Back-illuminated technology has been available for scientific CCD detectors for many years. Due to their higher sensitivity over a broader spectral region, back-illuminated detectors are preferred over front-illuminated detectors for low light applications. Front-illuminated sensors are reflective in appearance because most of the incident light is reflected back to the viewer, whereas back-illuminated sensors are visibly darker owing to their absorption of most of the incident light. As a result, sCMOS sensors are now capable of increased quantum efficiencies (>95%) without compromising low read noise and high frame rates [72].

Resolution MP	5 MP
Sensor size	2448*2048
Sensor format	2/3 “
Pixel size	3.45 µm
Max fps @ max ROI	77 fps
Quantum efficiency	0.67
Read noise	2.3 e-
Saturation capacity	10.7 ke-
Dynamic range	73 dB
SNR	40 dB

Table 3.2 Specifications of Baumer VCXU-50M camera

3.2.3 Noise and signal to noise ratio

In a real imaging system, noise is always present in the images. The intensity values that we measure are an approximation of the emitted or scattered photons by the sample. In what we measure. The variation of the signal during repeated observations is called noise. Noise induces uncertainty in our quantification of the intensity and hence uncertainty in the signal that has been measured. Photon counting can be modeled by a Poisson process [73] since the individual arrival of photons to the sensor can be treated as independent events that follow a random distribution. The number of photons N measured by a given element of a sensor over a time interval t is expressed by the discrete probability distribution function:

$$P_r(N = n) = \frac{e^{-ut}(ut)^k}{n!} \qquad \text{Eq. 3.4}$$

Where u is the expected number of photons per unit time interval and is proportional to the irradiance of the fluorophores in the sample. The parameter ut represents the expected incident photon count over the time interval. The uncertainty represented with this distribution is what we call photon or shot noise.

In a Poisson distribution, the variance of the random variable $\mathrm{Var}\,[N]$ is equal to its expectation, so $\mathrm{E}[N] = \mathrm{Var}\,[N] = ut$. This implies that photon noise is signal-dependent, i.e., the more photons collected, the more noise in the image, and its standard deviation grows with the square root of the signal, as shown in blue in Fig. 3.8.

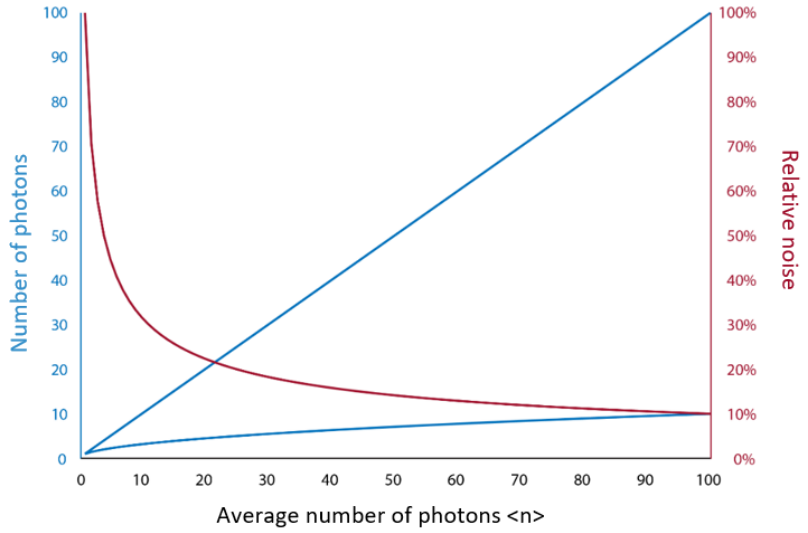

Fig. 3.8 The emission of photons by a fluorophore is random and can be modeled by a Poisson process. For an average of emitted photons, the variance scales with the signal strength as $\sqrt{ut}$. The relative noise decreases as the number of photons emitted increases.

When the available number of photons is low, noise is mainly influenced by other signal-independent sources [67]. For large photon counts, we can apply the central limit theorem and therefore model photon noise as a Gaussian distribution. In practice, photon noise is often modeled using a Gaussian distribution whose variance depends on the expected photon count,

$$N \sim \mathcal{N}(ut, ut)$$

Photon noise is due to the intrinsic uncertainty of the signal. Even in ideal conditions, using ideal electronics that would not input any type of noise, the measurements would still present photon noise. When imaging in conditions of high light, photon noise is the only significant source of noise, and the imaging is said to be photon-limited. To diminish photon noise, the strategy to follow is to increase the acquired signal. The ratio of photon noise to signal decays with the inverse of the square root of the number of photons captured, $\mathrm{noise/signal} \sim 1/\sqrt{ut}$. This means that photon noise, even though it grows in absolute terms with signal, is relatively lower at higher signal levels, as shown in red in Fig. 3.8.

If we wanted to increase the signal to noise ratio (SNR), that is, the signal magnitude relative to the uncertainty of the measurement, we would need to capture more photons. In this situation, the sample should be exposed for longer, and the number of photons captured finds its limit in

the full well capacity of the sensor. In digital sensors, there is a second source of noise that follows a Poisson distribution – dark current noise. It refers to artificial photon counts that are due to heating, which makes the sensor release electrons randomly. Photon noise is an inherent property of the signal, whereas dark current noise is derived from the sensor and depends on external properties like temperature or exposure time.

The variance of the camera pixel output is given by the sum of the variance of each noise source. The SNR, which is the ratio of the output signal to the standard deviation of the signal, is given by [74]:

$$SNR = \frac{PQ_e t}{\sqrt{PQ_e t + Dt + N_r^2}} \qquad \text{Eq. 3.5}$$

Where P is the incident photon flux (expressed in photons/pixel/s), Q_e is the quantum efficiency of the sensor, t is the exposure time (in seconds), D is thee dark current (electrons/pixel/second) and N_r represents the readout noise (electrons RMS/pixel). In this expression, the signal $PQ_e t$ is proportional to the number of photons emitted by the sample, the time of collection of those photons, and the quantum efficiency of the camera.

There noise term $\sqrt{PQ_e t + Dt + N_r^2}$ has three contributions. The first one is shot noise, which is proportional to the signal. The second one, dark noise, which increases with the time of integration. Finally, the electronics of a sensor are a source of noise for the signal. That is readout noise, which is defined as the uncertainty related to moving the electron charge within the sensor through the amplifier. Readout noise is the only source of noise that does not depend on exposure time.

Dark current D is typically around 1 e-/(px s) [75] and therefore negligible for short exposure times, as the ones considered in this work. Both readout noise and quantum efficiency are key properties of the sensors in this ponderation. In sensor terms, the Q_e is the probability that a photon is converted to an electron, and it is wavelength dependent.

Removing dark current from our consideration, we can rewrite the equation Eq. 3.5 as:

$$SNR = \frac{Q_e C_{\mathrm{p}}}{\sqrt{Q_e C_{\mathrm{p}} + N_r^2}} \qquad \text{Eq. 3.6}$$

Where $C_\mathrm{p} = P \cdot t$ is the total number of photons arriving the sensor or photon count. If we consider an ideal sensor, whose efficiency is total and does not supply any noise, only noise derived from the uncertainty of photons hitting the sensor would be present. In this case $Q_e = 1$ and $N_r = 0$, and the SNR would scale with the square root of the photon count, as depicted in Fig. 3.9. A typical sensor, nevertheless, has a quantum efficiency smaller than 1 and readout noise in the range of 1 to 3 e-. Next to the plot of the ideal sensor, we plotted the SNR of a sensor of $Q_e = 67$ and $N_r = 2.15$, values which correspond to the Baumer VCXU-50M camera, as shown in Table 3.3.

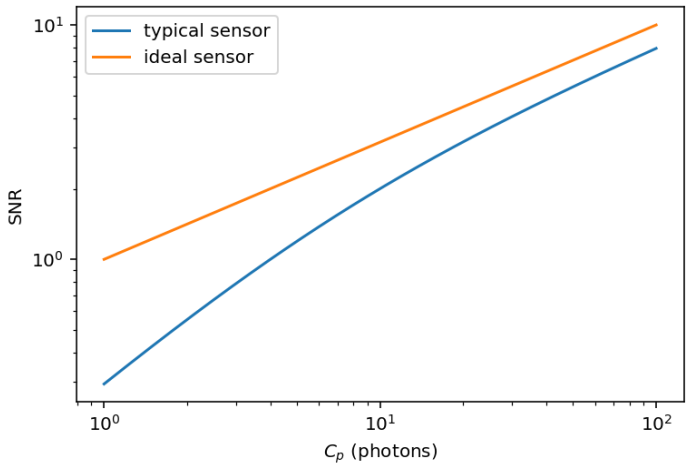

Fig. 3.9 SNR for an ideal and a typical sensor. In an ideal sensor with full quantum efficiency, $Q_e = 1$, and no readout noise, $N_r = 0$, the only source of noise is photon on shot noise, related to the uncertainty of photons to be emitted by the sample. SNR is therefore equal to the square root of the incident photons. In a real scenario $Q_e < 1$ and $N_r > 0$. The contribution of readout noise is greater at low light conditions, where the photon count C_p is low. The more photons emitted, the more the SNR resembles that of an ideal sensor.

Both parameters, of Q_e and N_r, influence image quality. The importance of each of the factors depends on the input light intensity. When illumination is low, the signal to noise ratio in a pixel is mainly influenced by readout noise. As the intensity rises, photon noise increases and the SNR starts to be defined by a combination of both types of noise. At higher intensities, only Q_e matters. One can already notice these two regimes for SNR in Fig. 3.9. The first one is the so-called low light region, where the readout noise is dominating, or $Q_e C_\mathrm{p} \ll N_r^2$. After that, the SNR resembles that of the ideal camera, where SNR is only dependent on $Q_e C_\mathrm{p}$.

Indeed, we can plot both sources of noise separately in Fig. 3.10 and see that the two curves for shot noise and readout noise cross for $C_\mathrm{p} \sim 8$ photons.

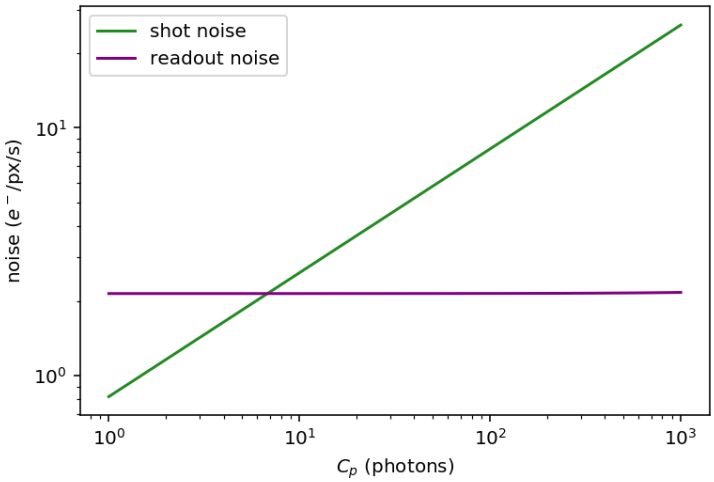

Fig. 3.10 Shot and readout noise at different light conditions. Readout noise is the predominant source of noise for low light conditions, whereas shot noise, which scales with the square root of the detected photons, is predominant when the photon count is high.

A summary of the specifications of some of the most popular cameras used for LSFM is presented in Table 3.3, along with the specifications for Baumer VCXU-50M, the camera used in this work.

Camera	Type	Qe	Nr(e-)	Shutter	#
PCO edge 5.5	sCMOS	0.6	2.3	Rolling	1
Baumer VCXU-50M	CMOS	0.67	2.15	Global	2
Photometrics Iris 15	sCMOS	0.73	1.5	Rolling	3
PCO Panda	sCMOS	0.8	2.3	Rolling	4
Hamamatsu Orca Fusion	sCMOS	0.8	1.4	Rolling	5
PCO edge 4.2	sCMOS	0.82	1.5	Rolling	6
Hamamatsu Orca Flash 4.0	sCMOS	0.82	1.6	Rolling	7
Andor Zyla 4	sCMOS	0.82	1.3	Rolling	8
Photometrics prime95b	sCMOS	0.95	1.8	Rolling	9

Table 3.3 Specifications of popular cameras used in LSFM along with the camera considered in this work, Baumer VCXU-50M.

The performance of these cameras in terms of SNR is very dependent on the number of photons that can be collected. This in turn depends on the brightness and the time of exposure, as explained in section 3.1.2. In the following graph, we present the SNR of the different cameras considered for two scenarios: with low light ($C_\mathrm{p} = 10$) and with ten times that amount and plot it in Fig. 3.11. The first thing we can observe is that the iso-SNR lines get more vertical with higher photon count – that is, at high photon count, Q_e is much more determinant than N_r.

This is not a surprise, since as explained earlier, readout noise has a bigger role at low light, whereas shot noise is more important in higher light conditions.

In the case of $C_{\mathrm{p}} = 10$, Photometrics Prime 95B gives the best performance with an SNR value of 2.74, a value which is 1.5x higher than that of the PCO edge 5.5 (with SNR=1.79). Interestingly, Andor Zyla 4, which offers a substantially lower Q_e (0.82 vs 0.95 in Prime 95 B) but a better readout noise (1.3 vs 1.8), gives an SNR of 2.61, very close to the 2.74 from Prime 95 B. This reinforces the belief that in conditions of low light, a slight improvement in readout noise has a comparable effect on image quality as pushing for quantum efficiency.

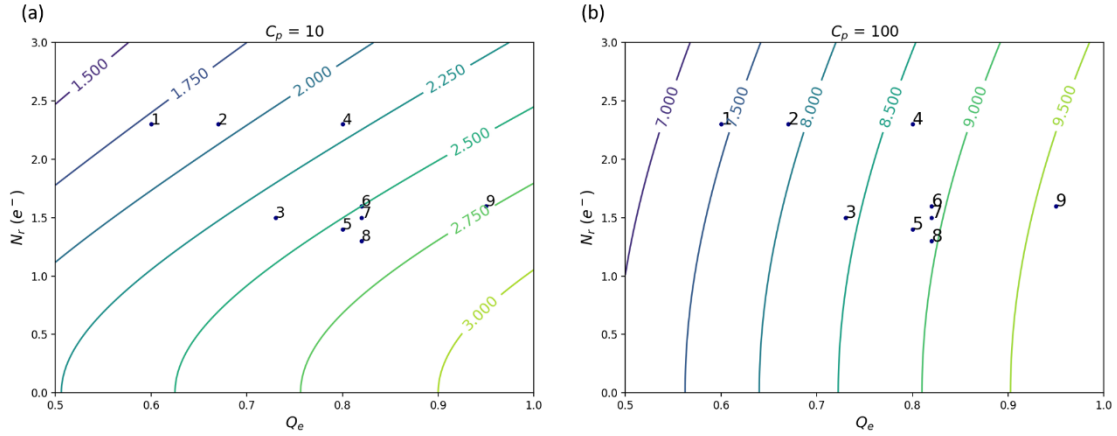

Fig. 3.11 SNR for the cameras listed in Table 3.3 for (a) a photon count of 10 photons and (b) 100 photons. Each camera is placed on the 2D space depending on its quantum efficiency and readout noise. Lines join points of equal SNR.

The camera used in this work, Baumer VCXU-50M gives an SNR of 1.93 and 7.88 for photon counts of 10 and 100 respectively. This is significantly lower than the values offered by Photometrics Prime 95B. Nevertheless, for a fair comparison, we should take into account that the global shutter greatly increases the time that signal is collected for every pixel. In global shutter cameras, no exposure time is lost for readout, whereas for full-frame readout, the sCMOS take 10ms. The gain in 10ms can be invested either in framerate – starting the acquisition of a new frame – or in increasing the exposure time, both options are shown in Fig. 3.13. This means that for the same framerate, a global shutter camera can acquire signal for 10ms more. For fast framerates the effect is substantial: a global shutter can deliver the same framerate collecting light for 11ms than an sCMOS collecting light for 1 ms, that is, it can collect 11 times as much light. Including the time for readout in the calculations, we can see the improvement in SNR when using a global shutter for high framerates (above 30 fps), as shown in Fig. 3.12.

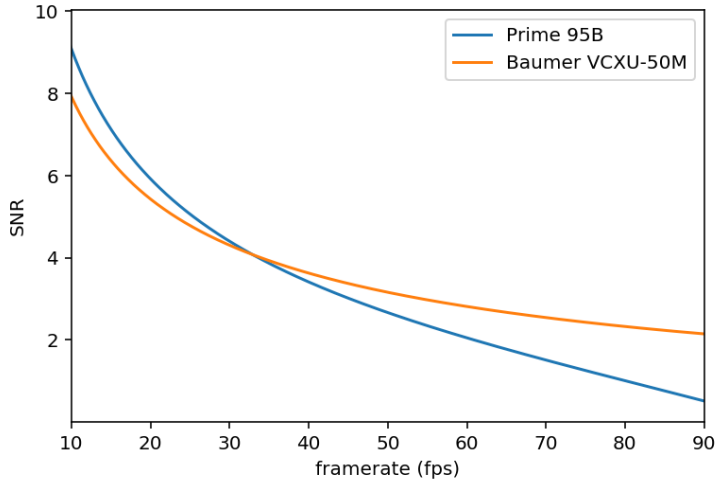

Fig. 3.12 SNR of Prime 95B and Baumer VCXU-50M at different framerates. Prime 95B performs better in terms of quantum efficiency and readout noise and therefore delivers higher SNR at low framerates. The global shutter of Baumer VCXU-50M permits longer exposure times than Prime 95B at equal framerates, which allows to collect more photons and increases SNR. A global shutter sensor with modest specifications can outperform a rolling shutter sensor with superior specifications when imaging at high framerates.

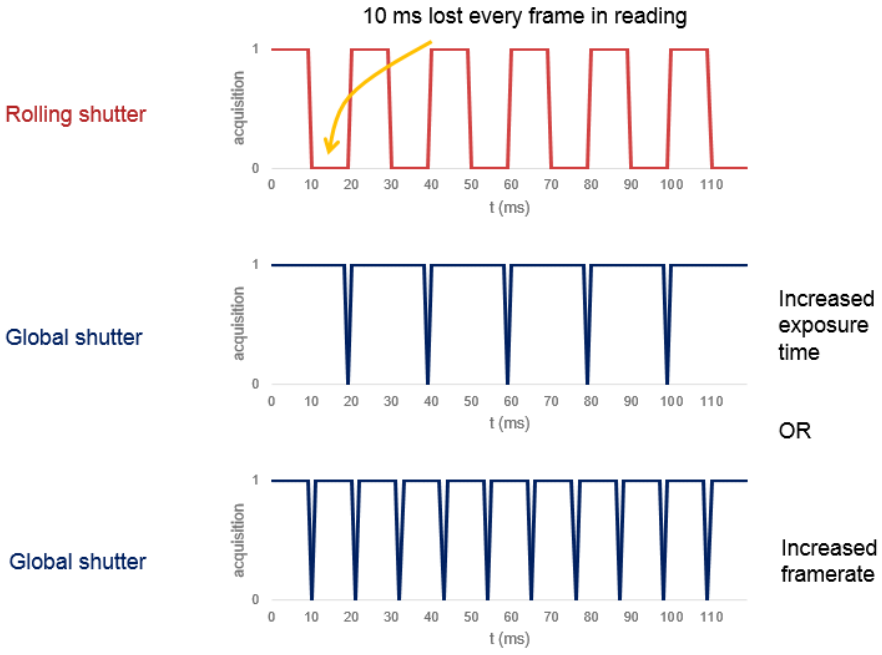

Fig. 3.13 A rolling shutter uses 10ms for readout. With this time, a global shutter can increase the exposure time while maintaining the same framerate, and therefore increase the signal detected. Alternatively, a global shutter can be used to increase the framerate with the same exposure time and therefore equal signal integrated.

3.3 The setup

The setup is conceived as an add-on to a Leica TCS SP8 DLS light-sheet microscope. In the TCS SP8 DLS, illumination light is focused by the illumination objective to form a light

sheet in the sample volume. Light from the sample is collected by the detection objective and focused by the tube lens onto one of the cameras. In our setup, a second camera is placed in the detection arm. We use a Baumer VCXU-50M camera with a global shutter (see full specification list in Table 3.2.

The camera is positioned in the place where the brightfield lamp normally is. We developed the camera adapter so that the microscope is fully backward compatible and the camera can be easily exchanged against the lamp at any time. The flip mirror that would normally allow selecting between brightfield illumination or the usual camera, allows selecting the camera that is used. A sketch of the setup along with a picture of the functioning setup can be found in Fig. 3.14.

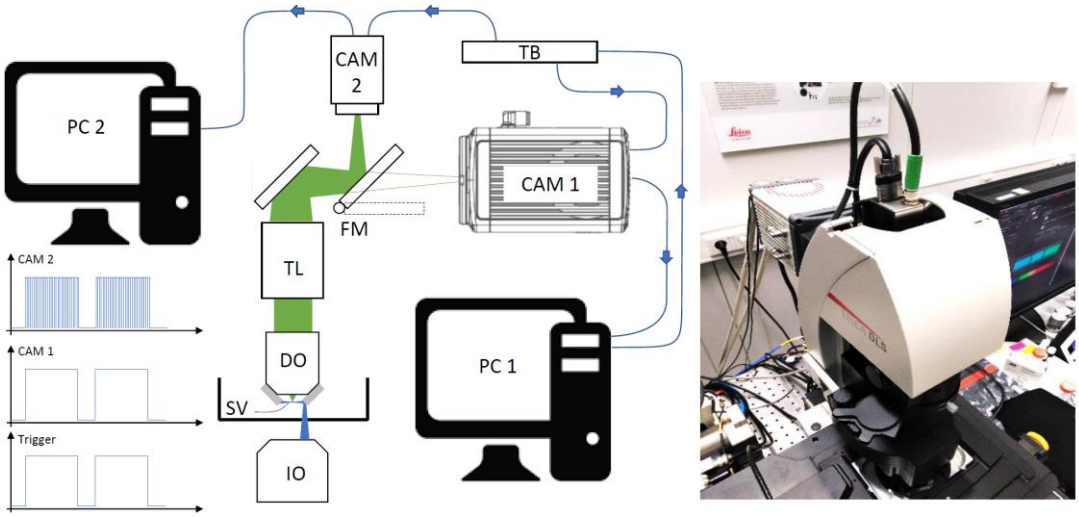

Fig. 3.14 Sketch of the setup. The illumination light is focused by the illumination objective (IO) to form a light sheet in the sample volume (SV). Light from the sample is collected by the detection objective (DO) and focused by the tube lens (TL) onto one of the cameras (CAM1, CAM2). The flip mirror (FM) allows to select the camera that is used A brightfield illumination lamp usually sits at the position of CAM 2, but the camera adapter that was developed to attach a second camera, CAM 2 to the microscope is fully backward compatible so that CAM 2 can be easily exchanged against the lamp at any time. CAM 1 is the Camera used with a regular Leica TCS SP8 DLS microscope. PC1 controls the microscope sends trigger signals to the camera via the trigger box and collects the image data from camera CAM1. CAM2 uses the same trigger signals as CAM1 but instead of acquiring a single frame runs at full speed recording multiple images during a single exposure of CAM1. CAM 2 is controlled by and streams the image data to a second computer, such as a notebook that runs a separate program written in LabVIEW to control the camera.

The camera is controlled by a custom-made LabVIEW code and synchronized with the microscope through trigger signals (see the user interface in LabVIEW in Fig. 3.16). One trigger signal is sent to the camera for a temporal series. Illumination is on during the whole series acquisition, even when the shutter is closed. The shutter is opened and closed for every frame

in the series. An additional computed is used for this task and the writing of the images. The data acquisition and saving run in parallel to prevent delays in the acquisition. The software is based on a two-loop – producer and consumer – that run continuously and in parallel. The first one loops over the camera to acquire the images in free-running mode. These images are directly transferred to a buffer, where they wait to be retrieved by the consumer loop. The consumer loop reads the images from the buffer and writes them to disk. The complete process can be visualized in Fig. 3.15. The Baumer camera is integrated with the LabVIEW software through USB3 Vision and GenICam standards.

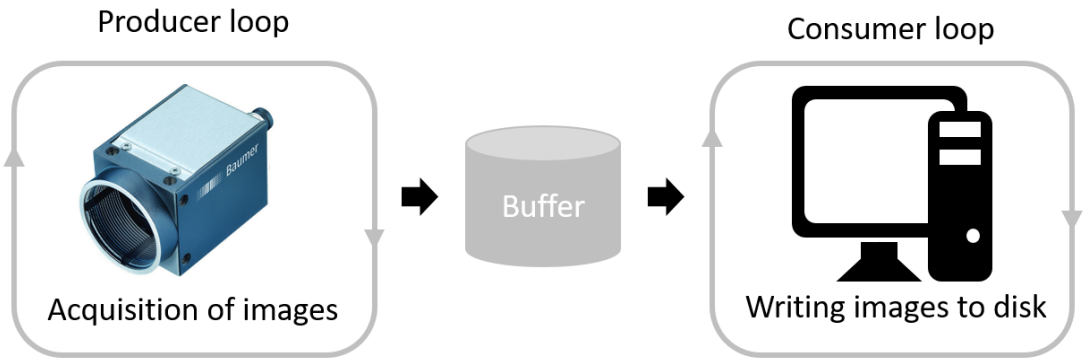

Fig. 3.15 Schematic of the image acquisition pipeline of our custom LabVIEW code. A producer loop loops over the camera. The images acquired are stored in a buffer to avoid delays in the acquisition. A consumer loop retrieves the images and writes them to disk.

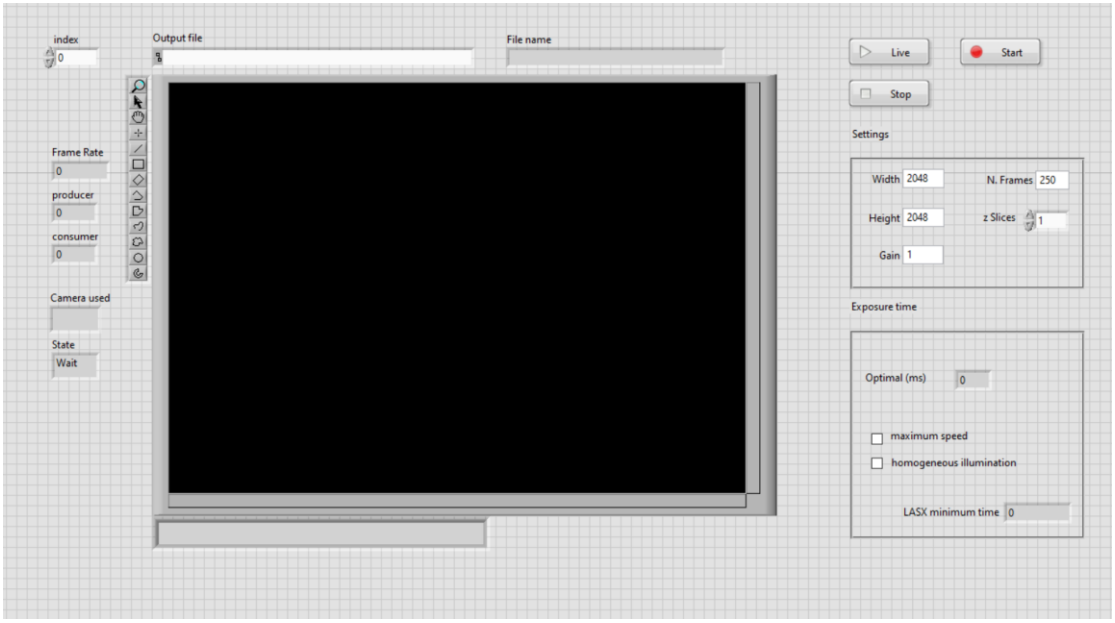

Fig. 3.16 User interface of the controlling software.

The use of this camera requires additional optics. The pixel size of the recommended cameras for Leica DLS is 6.5 µm. Here we are using a camera with a pixel size of 3.45 µm, which means that, for approximately the same number of pixels, the FOV will be almost 4x

smaller, and every pixel will get much less signal to integrate. For that reason, we place a lens that demagnifies the image in the path to the sensor.

The combination of the software with the camera enables imaging speeds of 77 fps at the full chip (2048 x 2048). Higher framerates can be acquired cropping the FOV, reaching over 600 fps, which is a significative improvement over the typical 120 fps limit of the microscope.

3.4 Setup tests and applications

The setup described in this thesis was used to image zebrafish embryos to analyze its performance.

On a first test, vasculature labeled (*fli:lifeAct-egfp*) zebrafish embryos were imaged at 48 hours post-fertilization (hpf). A volume stack was acquired with both the native setup of the microscope, containing a rolling shutter camera, and the setup developed in this work, with a global shutter camera. The goal was to assess the effect of the extra 10 ms on the image quality and noise level of the image. The exposure time was therefore set for i) 10ms for the rolling shutter camera and 20 ms for the global shutter camera and ii) 1 ms for the rolling shutter camera and 10ms for the global shutter camera. The resulting images are shown in Fig. 3.17.

On a second test, each camera was set to take a video of the endocardium of the beating zebrafish heart at 48hpf. The framerate was kept constant at 100 fps. On the native setup, the exposure time was set to 1 ms to keep the framerate at that level, while on the custom-made setup presented in this work, the exposure time could be increased to 10 ms to keep the same framerate. A capture of the intensity profile along the yellow line is plotted to show the difference in contrast in Fig. 3.18. With the global shutter camera, the base intensity is lower and the intensity peaks are higher. The noise is overall lower. This shows the increase in signal quality due to the extra illumination time with a global shutter camera.

The camera was also tested on recordings of (1) the respective movement of endocardium and myocardium of a 52 hpf zebrafish embryo *(fli:lifeAct-efgp;cmlc2:gal4FF;UAS:RFP)* at 290 fps, (2) the movement of red blood cells through an artery in a zebrafish embryo at 70 hpf (*fli:lifeAct-egfp)* at 450 fps and (3) the flow of red blood cells through the atrioventricular canal on a 52 hpf zebrafish heart (*fli:lifeAct-egfp)* at 290 fps. See the videos attached.

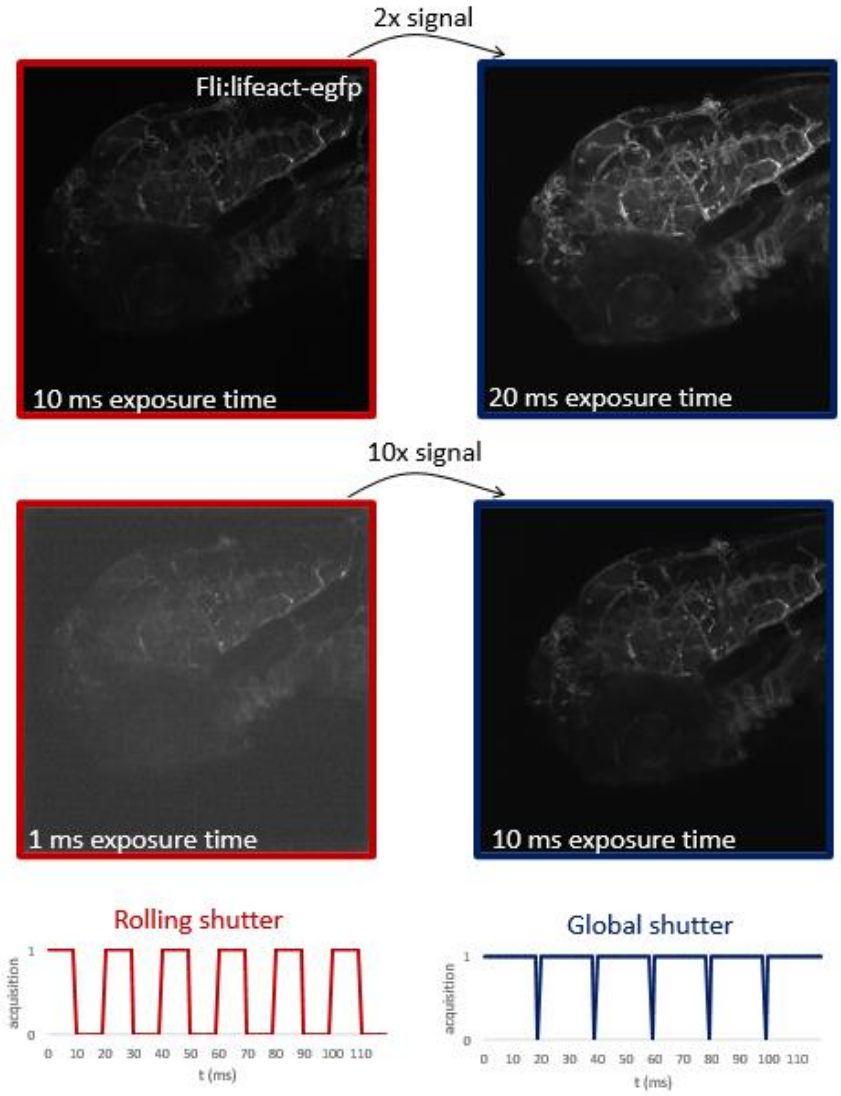

Fig. 3.17 Comparison of the global and rolling shutter cameras. The 10 ms that the native rolling shutter camera uses for readout can be used for exposure in the custom-made global shutter setup. In the case of 10 ms exposure time, the amount of integrated signal doubles, whereas in the case of 1 ms exposure time, the signal is multiplied tenfold.

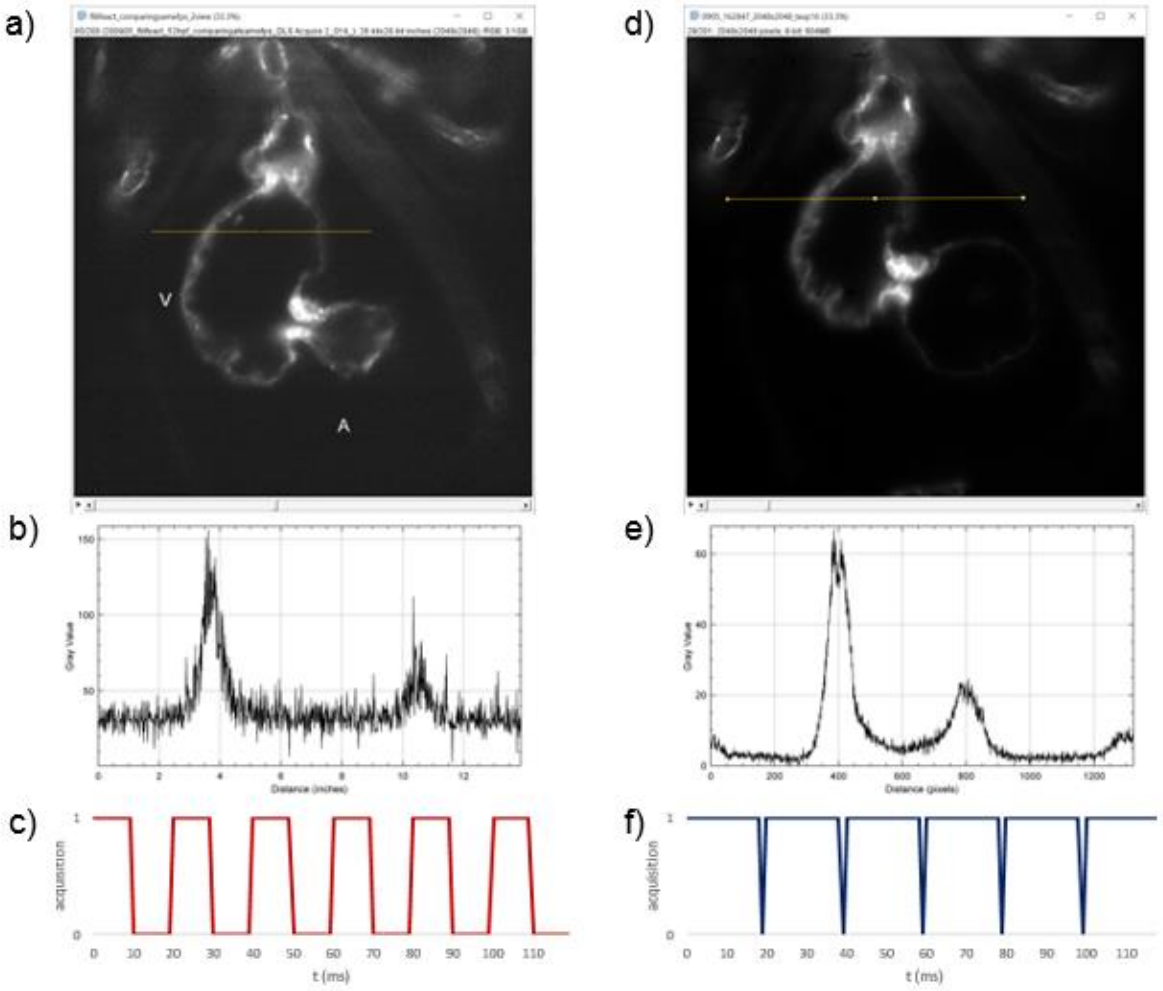

Fig. 3.18 Comparison of the global and rolling shutter cameras for equal framerate. The endocardium of a fli:lifeAct-egfp zebrafish embryo of at 48 hpf is imaged at a framerate of 100 fps with (a – c) the native rolling shutter camera and (d – f) the custom setup with a global shutter camera. To achieve that acquisition speed with the native rolling shutter camera, the exposure time has to be set to 1 ms, whereas with the custom setup and global shutter camera, the exposure time is set to 10 ms. (a. d) A frame is shown in both cases showing the atrium (A) and the ventricle (V). (b, e) The resulting intensity profiles along the yellow lines are plotted, showing the improvement in SNR due to the longer exposure time in the global shutter camera. (c, f) schematic of the exposure vs time for a rolling and a global shutter camera.

Discussion and conclusions

The work presented in this thesis contributes to the understanding of the effect of light-sheet thickness and geometry on the resolution and contrast of the images that can be obtained with it. The results of the simulations of propagation of beams presented in this dissertation show that, against what was claimed in some publications before, axial resolution in light-sheet can only be improved at the expense of optical sectioning, and viceversa. In other words, there is an unavoidable trade-off between axial resolution and optical sectioning in light-sheet. The work presented here is also aimed at offering tools to decide what light-sheet is best depending on the application.

The simulations presented do not however take into account the effects of scattering introduced by the sample. The stability of the different beams upon propagation differs, as it has been shown in literature [5,7,38]. Self-healing beams, like Bessel beams and Airy beams, reconstruct themselves after encountering an obstacle. This property makes them more suitable for imaging inside highly-scattering samples, since their beam shape is assumed to be more conserved upon propagation inside those samples. How much this can affect the effective resolution and optical sectioning remains to be analyzed and is left for future work.

The simulator presented in this work was developed to evaluate the geometry – in particular the thickness – of light-sheet fluorescence microscopy schemes found in literature. It also offers the possibility to measure any light-sheet imagined by the user, as long as the images of the electrical field intensity and phase are provided. The Light Sheet Simulator software is available for download at https://github.com/remachae/beamsimulator. The repository includes all the source codes and a user manual.

On the second part of this work, the challenges of imaging at high speed are discussed. In particular, this work focuses on the choice of sensors and shutters and their effect on signal to noise ratio. The possibilities of using a global shutter back-illuminated CMOS camera with a scanned beam light-sheet are discussed. In particular, the possibilities of integrating a modest and cheap camera into a commercial microscope to push the possibilities in terms of speed of acquisition. The potential of the setup is showcased by different examples in the context of cardiovascular imaging of developing zebrafish embryos.

Bibliography

1. J. Huisken, J. Swoger, F. Del Bene, J. Wittbrodt, and E. H. K. Stelzer, "Optical Sectioning Deep Inside Live Embryos by Selective Plane Illumination Microscopy," Science **305**, 1007 (2004).

2. J. Huisken and D. Y. R. Stainier, "Selective plane illumination microscopy techniques in developmental biology," Development **136**, 1963–1975 (2009).

3. M. Weber, N. Scherf, A. M. Meyer, D. Panáková, P. Kohl, and J. Huisken, "Cell-accurate optical mapping across the entire developing heart.," Elife **6**, (2017).

4. F. O. Fahrbach, V. Gurchenkov, K. Alessandri, P. Nassoy, and A. Rohrbach, "Self-reconstructing sectioned Bessel beams offer submicron optical sectioning for large fields of view in light-sheet microscopy.," Opt Express **21**, 11425–11440 (2013).

5. T. Vettenburg, H. I. C. Dalgarno, J. Nylk, C. Coll-Lladó, D. E. K. Ferrier, T. Čižmár, F. J. Gunn-Moore, and K. Dholakia, "Light-sheet microscopy using an Airy beam," Nature Methods **11**, 541–544 (2014).

6. B.-C. Chen, W. R. Legant, K. Wang, L. Shao, D. E. Milkie, M. W. Davidson, C. Janetopoulos, X. S. Wu, J. A. Hammer, Z. Liu, B. P. English, Y. Mimori-Kiyosue, D. P. Romero, A. T. Ritter, J. Lippincott-Schwartz, L. Fritz-Laylin, R. D. Mullins, D. M. Mitchell, J. N. Bembenek, A.-C. Reymann, R. Böhme, S. W. Grill, J. T. Wang, G. Seydoux, U. S. Tulu, D. P. Kiehart, and E. Betzig, "Lattice light-sheet microscopy: Imaging molecules to embryos at high spatiotemporal resolution," Science **346**, 1257998 (2014).

7. F. O. Fahrbach, P. Simon, and A. Rohrbach, "Microscopy with self-reconstructing beams," Nature Photonics **4**, 780 (2010).

8. M. Weber and J. Huisken, "In vivo imaging of cardiac development and function in zebrafish using light sheet microscopy.," Swiss Med Wkly **145**, w14227 (2015).

9. T. V. Truong, W. Supatto, D. S. Koos, J. M. Choi, and S. E. Fraser, "Deep and fast live imaging with two-photon scanned light-sheet microscopy," Nat Methods **8**, 757–760 (2011).

10. V. Trivedi, T. V. Truong, L. A. Trinh, D. B. Holland, M. Liebling, and S. E. Fraser, "Dynamic structure and protein expression of the live embryonic heart captured by," Biomed Opt Express **6**, 2056–2066 (2015).

11. P. Mahou, J. Vermot, E. Beaurepaire, and W. Supatto, "Multicolor two-photon light-sheet microscopy," Nat Methods **11**, 600–601 (2014).

12. E. J. Gualda, D. Simão, C. Pinto, P. M. Alves, and C. Brito, "Imaging of human differentiated 3D neural aggregates using light sheet fluorescence microscopy.," Front Cell Neurosci **8**, 221 (2014).

13. E. J. Gualda, T. Vale, P. Almada, J. A. Feijó, G. G. Martins, and N. Moreno, "OpenSpinMicroscopy: an open-source integrated microscopy platform.," Nat Methods **10**, 599–600 (2013).

14. E. J. Gualda, H. Pereira, T. Vale, M. F. Estrada, C. Brito, and N. Moreno, "SPIM-fluid: open source light-sheet based platform for high-throughput imaging.," Biomed Opt Express **6**, 4447–4456 (2015).

15. P. G. Pitrone, J. Schindelin, L. Stuyvenberg, S. Preibisch, M. Weber, K. W. Eliceiri, J. Huisken, and P. Tomancak, "OpenSPIM: an open-access light-sheet microscopy platform.," Nat Methods **10**, 598–599 (2013).

16. P. J. Keller and E. H. K. Stelzer, "Quantitative in vivo imaging of entire embryos with Digital Scanned Laser Light Sheet Fluorescence Microscopy.," Curr Opin Neurobiol **18**, 624–632 (2008).

17. A. Rohrbach, "Artifacts resulting from imaging in scattering media: a theoretical prediction," Optics Letters **34**, 3041 (2009).

18. P. J. Keller, A. D. Schmidt, A. Santella, K. Khairy, Z. Bao, J. Wittbrodt, and E. H. K. Stelzer, "Fast, high-contrast imaging of animal development with scanned light sheet–based structured-illumination microscopy," Nature Methods **7**, 637–642 (2010).

19. R. Heintzmann and T. Huser, "Super-Resolution Structured Illumination Microscopy," Chem. Rev. **117**, 13890–13908 (2017).

20. A. Marcos-Vidal and J. Ripoll, "Recent advances in optical tomography in low scattering media," Optics and Lasers in Engineering 106191 (2020).

21. J. Huisken and D. Y. R. Stainier, "Even fluorescence excitation by multidirectional selective plane illumination microscopy (mSPIM)," Opt. Lett. **32**, 2608 (2007).

22. X. Peng, X. Huang, K. Du, H. Liu, and L. Chen, "High spatiotemporal resolution and low photo-toxicity fluorescence imaging in live cells and in vivo.," Biochem Soc Trans **47**, 1635–1650 (2019).

23. U. Krzic, S. Gunther, T. E. Saunders, S. J. Streichan, and L. Hufnagel, "Multiview light-sheet microscope for rapid in toto imaging," Nat Methods **9**, 730–733 (2012).

24. S. Preibisch, S. Saalfeld, J. Schindelin, and P. Tomancak, "Software for bead-based registration of selective plane illumination microscopy data," Nature Methods **7**, 418–419 (2010).

25. S. Preibisch, F. Amat, E. Stamataki, M. Sarov, R. H. Singer, E. Myers, and P. Tomancak, "Efficient Bayesian-based multiview deconvolution," Nature Methods **11**, 645–648 (2014).

26. Y. Wu, A. Ghitani, R. Christensen, A. Santella, Z. Du, G. Rondeau, Z. Bao, D. Colon-Ramos, and H. Shroff, "Inverted selective plane illumination microscopy (iSPIM) enables coupled cell identity lineaging and neurodevelopmental imaging in Caenorhabditis elegans," Proceedings of the National Academy of Sciences **108**, 17708–17713 (2011).

27. E. Reynaud, J. Peychl, J. Huisken, and P. Tomancak, "Guide to light-sheet microscopy for adventurous biologists," Nature methods **12**, 30–4 (2014).

28. A. K. Glaser, N. P. Reder, Y. Chen, E. F. McCarty, C. Yin, L. Wei, Y. Wang, L. D. True, and J. T. C. Liu, "Light-sheet microscopy for slide-free non-destructive pathology of large clinical specimens.," Nat Biomed Eng **1**, (2017).

29. R. McGorty, H. Liu, D. Kamiyama, Z. Dong, S. Guo, and B. Huang, "Open-top selective plane illumination microscope for conventionally mounted specimens.," Opt Express **23**, 16142–16153 (2015).

30. T. C. Fadero, T. M. Gerbich, K. Rana, A. Suzuki, M. DiSalvo, K. N. Schaefer, J. K. Heppert, T. C. Boothby, B. Goldstein, M. Peifer, N. L. Allbritton, A. S. Gladfelter, A. S. Maddox, and P. S. Maddox, "LITE microscopy: Tilted light-sheet excitation of model organisms offers high resolution and low photobleaching.," J Cell Biol **217**, 1869–1882 (2018).

31. A.-K. Gustavsson, P. N. Petrov, M. Y. Lee, Y. Shechtman, and W. E. Moerner, "Tilted Light Sheet Microscopy with 3D Point Spread Functions for Single-Molecule Super-Resolution Imaging in Mammalian Cells.," Proc SPIE Int Soc Opt Eng **10500**, (2018).

32. V. Voleti, K. B. Patel, W. Li, C. Perez Campos, S. Bharadwaj, H. Yu, C. Ford, M. J. Casper, R. W. Yan, W. Liang, C. Wen, K. D. Kimura, K. L. Targoff, and E. M. C. Hillman, "Real-time volumetric microscopy of in vivo dynamics and large-scale samples with SCAPE 2.0," Nature Methods **16**, 1054–1062 (2019).

33. C. Dunsby, "Optically sectioned imaging by oblique plane microscopy," 11 (2008).

34. F. Cutrale and E. Gratton, "Inclined selective plane illumination microscopy adaptor for conventional microscopes.," Microsc Res Tech **75**, 1461–1466 (2012).

35. M. B. Bouchard, V. Voleti, C. S. Mendes, C. Lacefield, W. B. Grueber, R. S. Mann, R. M. Bruno, and E. M. C. Hillman, "Swept confocally-aligned planar excitation (SCAPE) microscopy for high-speed volumetric imaging of behaving organisms," Nature Photon **9**, 113–119 (2015).

36. K. M. Dean, P. Roudot, E. S. Welf, G. Danuser, and R. Fiolka, "Deconvolution-free Subcellular Imaging with Axially Swept Light Sheet Microscopy," Biophysical Journal **108**, 2807–2815 (2015).

37. K. M. Dean, P. Roudot, C. R. Reis, E. S. Welf, M. Mettlen, and R. Fiolka, "Diagonally Scanned Light-Sheet Microscopy for Fast Volumetric Imaging of Adherent Cells.," Biophys J **110**, 1456–1465 (2016).

38. T. A. Planchon, L. Gao, D. E. Milkie, M. W. Davidson, J. A. Galbraith, C. G. Galbraith, and E. Betzig, "Rapid three-dimensional isotropic imaging of living cells using Bessel beam plane illumination," Nat Methods **8**, 417–423 (2011).

39. "Gaussian Beam Optics," in *Photonics and Lasers* (John Wiley & Sons, Ltd, 2006), pp. 307–325.

40. R. Tomer, M. Lovett-Barron, I. Kauvar, A. Andalman, V. M. Burns, S. Sankaran, L. Grosenick, M. Broxton, S. Yang, and K. Deisseroth, "SPED Light Sheet Microscopy: Fast Mapping of Biological System Structure and Function," Cell **163**, 1796–1806 (2015).

41. O. E. Olarte, J. Andilla, D. Artigas, and P. Loza-Alvarez, "Decoupled illumination detection in light sheet microscopy for fast volumetric imaging," Optica **2**, 702 (2015).

42. B.-J. Chang, K. M. Dean, and R. Fiolka, "Systematic and quantitative comparison of lattice and Gaussian light-sheets," Opt. Express **28**, 27052 (2020).

43. O. E. Olarte, J. Andilla, E. J. Gualda, and P. Loza-Alvarez, "Light-sheet microscopy: a tutorial," Advances in Optics and Photonics **10**, 111 (2018).

44. J. Vermot, S. E. Fraser, and M. Liebling, "Fast fluorescence microscopy for imaging the dynamics of embryonic development," HFSP Journal **2**, 143–155 (2008).

45. G. U. Nienhaus and K. Nienhaus, "Fluorescence Labeling," in *Fluorescence Microscopy*, U. Kubitscheck, ed. (Wiley-VCH Verlag GmbH & Co. KGaA, 2017), pp. 133–164.

46. J. Icha, M. Weber, J. C. Waters, and C. Norden, "Phototoxicity in live fluorescence microscopy, and how to avoid it.," Bioessays **39**, (2017).

47. J. Icha, C. Kunath, M. Rocha-Martins, and C. Norden, "Independent modes of ganglion cell translocation ensure correct lamination of the zebrafish retina," Journal of Cell Biology **215**, 259–275 (2016).

48. P. Strnad, S. Gunther, J. Reichmann, U. Krzic, B. Balazs, G. de Medeiros, N. Norlin, T. Hiiragi, L. Hufnagel, and J. Ellenberg, "Inverted light-sheet microscope for imaging mouse pre-implantation development.," Nat Methods **13**, 139–142 (2016).

49. P. M. Carlton, J. Boulanger, C. Kervrann, J.-B. Sibarita, J. Salamero, S. Gordon-Messer, D. Bressan, J. E. Haber, S. Haase, L. Shao, L. Winoto, A. Matsuda, P. Kner, S. Uzawa, M. Gustafsson, Z. Kam, D. A. Agard, and J. W. Sedat, "Fast live simultaneous multiwavelength four-dimensional optical microscopy," Proceedings of the National Academy of Sciences **107**, 16016–16022 (2010).

50. M. Jemielita, M. J. Taormina, A. DeLaurier, C. B. Kimmel, and R. Parthasarathy, "Comparing phototoxicity during the development of a zebrafish craniofacial bone using confocal and light sheet fluorescence microscopy techniques: Comparing light sheet and confocal derived phototoxicity in bone development," Journal of Biophotonics **6**, 920–928 (2013).

51. K. Yamagata, R. Suetsugu, and T. Wakayama, "Long-Term, Six-Dimensional Live-Cell Imaging for the Mouse Preimplantation Embryo That Does Not Affect Full-Term Development," Journal of Reproduction and Development **55**, 343–350 (2009).

52. C. Boudreau, T.-L. (Erika) Wee, Y.-R. (Silvia) Duh, M. P. Couto, K. H. Ardakani, and C. M. Brown, "Excitation Light Dose Engineering to Reduce Photo-bleaching and Photo-toxicity," Scientific Reports **6**, (2016).

53. J. M. Murray, P. L. Appleton, J. R. Swedlow, and J. C. Waters, "Evaluating performance in three-dimensional fluorescence microscopy," Journal of Microscopy **228**, 390–405 (2007).

54. M. Mickoleit, B. Schmid, M. Weber, F. O. Fahrbach, S. Hombach, S. Reischauer, and J. Huisken, "High-resolution reconstruction of the beating zebrafish heart," Nature Methods **11**, 919–922 (2014).

55. P. J. Keller and M. B. Ahrens, "Visualizing whole-brain activity and development at the single-cell level using light-sheet microscopy.," Neuron **85**, 462–483 (2015).

56. S. Daetwyler and J. Huisken, "Fast Fluorescence Microscopy with Light Sheets.," Biol Bull **231**, 14–25 (2016).

57. T. F. Holekamp, D. Turaga, and T. E. Holy, "Fast three-dimensional fluorescence imaging of activity in neural populations by objective-coupled planar illumination microscopy.," Neuron **57**, 661–672 (2008).

58. D. Turaga and T. E. Holy, "Organization of vomeronasal sensory coding revealed by fast volumetric calcium imaging.," J Neurosci **32**, 1612–1621 (2012).

59. W. C. Lemon, S. R. Pulver, B. Höckendorf, K. McDole, K. Branson, J. Freeman, and P. J. Keller, "Whole-central nervous system functional imaging in larval Drosophila.," Nat Commun **6**, 7924 (2015).

60. F. O. Fahrbach, F. F. Voigt, B. Schmid, F. Helmchen, and J. Huisken, "Rapid 3D light-sheet microscopy with a tunable lens," Opt. Express **21**, 21010 (2013).

61. E. J. Botcherby, R. Juskaitis, M. J. Booth, and T. Wilson, "Aberration-free optical refocusing in high numerical aperture microscopy.," Opt Lett **32**, 2007–2009 (2007).

62. S. Kumar, D. Wilding, M. B. Sikkel, A. R. Lyon, K. T. MacLeod, and C. Dunsby, "High-speed 2D and 3D fluorescence microscopy of cardiac myocytes," Optics Express **19**, 13839 (2011).

63. M. Levoy, R. Ng, A. Adams, M. Footer, and M. Horowitz, "Light Field Microscopy," in *ACM SIGGRAPH 2006 Papers*, SIGGRAPH '06 (Association for Computing Machinery, 2006), pp. 924–934.

64. R. Prevedel, Y.-G. Yoon, M. Hoffmann, N. Pak, G. Wetzstein, S. Kato, T. Schrödel, R. Raskar, M. Zimmer, E. S. Boyden, and A. Vaziri, "Simultaneous whole-animal 3D imaging of neuronal activity using light-field microscopy," Nature Methods **11**, 727–730 (2014).

65. T. V. Truong, D. B. Holland, S. Madaan, A. Andreev, K. Keomanee-Dizon, J. V. Troll, D. E. S. Koo, M. J. McFall-Ngai, and S. E. Fraser, "High-contrast, synchronous volumetric imaging with selective volume illumination microscopy," Commun Biol **3**, 74 (2020).

66. J. Joubert and D. Sharma, "Light Microscopy Digital Imaging," Current Protocols in Cytometry **58**, (2011).

67. T. J. Lambert and J. C. Waters, "Assessing camera performance for quantitative microscopy," in *Methods in Cell Biology* (Elsevier, 2014), Vol. 123, pp. 35–53.

68. "EMCCD vs. sCMOS for Microscopic Imaging," https://www.photonics.com/Articles/EMCCD_vs_sCMOS_for_Microscopic_Imaging/a46174.

69. "CMOS Image Sensor," in *CMOS Integrated Lab-on-a-Chip System for Personalized Biomedical Diagnosis* (John Wiley & Sons Singapore Pte. Ltd, 2018), pp. 142–168.

70. M. Baker, "Faster frames, clearer pictures," Nature Methods **8**, 1005–1009 (2011).

71. D. Lappenküper, "Sensor Comparison: Are All IMXs Equal?," https://vision.i2s.fr/img/cms/BAS1711_White_Paper_IMX-Comparison.pdf.

72. Justin Cooper, Alan Mullan, Aleksandra Marsh, and Marcin Barszczewski, "Characterization of performance of back-illuminated SCMOS cameras versus conventional SCMOS and EMCCD cameras for microscopy applications," in (2019), Vol. 10925.

73. "Poisson Processes and Shot Noise," in *Introduction to Random Signals and Noise* (John Wiley & Sons, Ltd, 2006), pp. 193–210.

74. S. Fullerton, K. Bennett, E. Toda, and T. Takahashi, "Optimization of precision localization microscopy using CMOS camera technology," in J. Enderlein, Z. K. Gryczynski, R. Erdmann, F. Koberling, and I. Gregor, eds. (2012), p. 82280T.

75. "Camera Noise and Temperature Tutorial," (n.d.).

76. B.-J. Chang, K. M. Dean, and R. Fiolka, *A Systematic and Quantitative Comparison of Lattice and Gaussian Light-Sheets* (Biophysics, 2020).

Elena REMACHA MOTTA

Développement de stratégies de microscopie pour l'imagerie rapide du développement du cœur du poisson-zèbre

Résumé

Les structures au cœur du poisson-zèbre sont très dynamiques et couvrent un large éventail des échelles et des vitesses. La technique de microscopie qui répond le mieux aux défis posés par l'imagerie de la morphogenese cardiaque est la microscopie en feuillet de luniere (Light Sheet Fluorescence Microscopy ou LSFM). LSFM a gagné en popularité, ce qui a genere un grand nombre d'approche et de montage optique permettant de créer des feuillets de lumiere avec des proprietes tres differentes. Pourtant, aucune comparaison détaillée et objective entre tous les types de feuilles de lumière ont été réalisés. Pour combler cette lacune, nous avons décrit un ensemble de mesures et avons comparé les different types de feuillet de lumieres existants.

D'un otre cote, notre groupe s'intéresse aux processus très dynamiques du cœur. Nous avons developpe et mis en place une solution modulaire à attacher au Leica DLS Light Sheet disponible à l'institut qui nous permettrait d'acquérir des images avec une haute résolution temporelle.

Résumé en anglais

Structures inside the heart of zebrafish are highly dynamic, and span a broad range of and scales and velocities. The microscopy technique that best addresses the challenges posed by cardiac imaging is Light Sheet Fluorsescence Microscopy (LSFM). LSFM has only gained popularity since its introduction in biological research, which has led to the development of many techniques aiming at making the perfect light sheet. Yet, not a detailed and objective comparison between all the types of light sheets have been made. To fill this gap, we described a set of measures and compared the existing LSFM schemes.

Our group is interested in the very dynamic processes in the heart. For that, we decided to implement a modular solution to attach to the Leica DLS Light Sheet system available in the institute that allows us to acquire images with high temporal resolution.